Strål
säkerhets
myndigheten
Swedish Radiation Safety Authority

Author: Tobias Bolinder

Research

2014:28

Numerical simulation of ductile crack growth in residual stress fields

Report number: 2014:28 ISSN: 2000-0456
Available at www.stralsakerhetsmyndigheten.se

SSM perspective

Background

Components in nuclear power plants are usually subjected to loads causing both primary and secondary stresses. ASME XI code and the R6 procedure, which are commonly used for assessment of cracked components, treat the issue of secondary stresses differently. The R6-method tends to give overly conservative results, while the ASME XI code does not consider weld-induced residual stresses in some materials.

A previous analytical study (SSM research report 2009:27) was aimed at investigating the significance of the secondary stresses for cracks in ductile materials within nuclear applications. The main contribution to secondary stresses is usually weld residual stresses. In that study a deterministic safety evaluation procedure was proposed in which the residual stresses were weighted down for ductile materials. The proposed safety evaluation procedure for treatment of certain secondary stresses for ductile materials has been verified experimentally in a subsequent study (SSM research report 2011:19).

Objectives

The objective of the project is to evaluate the ability of the so-called Gurson model in predicting the effect from load history and residual stresses as a first step to be able to simulate ductile initiation and tearing in situations with high residual stresses. The study includes an experimental program as well as numerically modeling of performed experiments.

Results

The study has shown on the capability of the cell model in capturing the effects on ductile tearing from limited pre-load levels and a residual stress field.

Some of the conclusions are as follows:

- No distinctive influence on the material fracture toughness is observed from pre-loading (work hardening), both tensile and compressive, at room temperature of 1.5 or 3 % total strain.
- The cell model gives good predictions of the experimentally generated JR-curves for pre-load levels up to 3% in compression and tension. As for the experimental results, no significant effect from the pre-load on the fracture resistance is seen for pre-load levels up to 3%.
- The predicted results overestimate the material fracture toughness for pre-load levels of 6%. The seen effect from the experimental results at a pre-load level of 6% is much larger than the predicted effect both for compression and tension. The current cell model fails therefore to accurately capture the large effects seen at higher levels of pre-load.
- The results show the capability of the so-called Gurson model to capture the increased fracture toughness compared to the standard specimen which is due to constraint effects.

Need for further research

Complementary experiments are needed to be conducted in order to get a deeper understanding of the behavior for the used material. A modified Gurson model which takes in to account the void growth at low triaxiality and shear dominated states needs to be used to potentially get more accurate predictions of the JR-curves and the shape of the crack front.

Project information

Contact person SSM: Kostas Xanthopoulos
Reference: SSM 2010/4177

Strål
säkerhets
myndigheten
Swedish Radiation Safety Authority

Authors: Tobias Bolinder
Inspecta Technology AB

2014:28

Numerical simulation of ductile crack growth in residual stress fields

Date: May 2014
Report number: 2014:28 ISSN: 2000-0456
Available at www.stralsakerhetsmyndigheten.se

This report concerns a study which has been conducted for the Swedish Radiation Safety Authority, SSM. The conclusions and viewpoints presented in the report are those of the author/authors and do not necessarily coincide with those of the SSM.

Summary

In this report, the project “Numerical simulation of ductile crack growth in residual stress fields” will be presented. In the project an experimental program together with numerical cell modeling have been conducted. The material used in the experiments was A533B-1.

From the experimentally evaluated J_R-curves, a large effect on the material fracture toughness is seen for specimens pre-loaded to 6% total strain. This is true for pre-loading in both tension and compression but the effect is larger in the specimens pre-loaded in tension. It can also be concluded that no distinctive effects on J_{Ic} is seen from pre-loading to 1.5 or 3 % total strain. It should be noted that the effects seen, as a result of work hardening, are due to a prior pre-load at room temperature. Hence these effects are not representable for cases were the material exhibits a level of pre-strain caused by welding.

In the computational part of the project the scheme outlined by Faleskog et al. [1] and Gao et al. [2] to determine the material parameters, for the cell model, based on a uniaxial tensile test and a standard fracture test is shown to be a structured and sound approach.
The cell model gives good predictions of the experimentally generated J_R-curves for pre-load levels up to 3% in compression and tension. But it fails to accurately capture the Load-CMOD curves and the large effects seen at high levels of pre-load on the J_R-curves. It is probable that this could be rectified by a cell model using a kinematic material hardening.
The cell model does capture the effects attributable to residual stresses, seen in the experimental work by Bolinder et al. [3], in regards to the load-CMOD curve, fracture toughness and the decreasing influence on the J-integral for increasing primary load.
The predicted J_R-curves for the nonstandard specimens with and without residual stresses lie on the upper bound of the experimental scatter, slightly overestimating the fracture toughness. This can be rectified by using a modified Gurson model which takes into account the void growth at low triaxiality and shear dominated states.

The report has shown on the capability of the cell model in capturing the effects on ductile tearing from limited pre-load levels and a residual stress field. Nevertheless there have also been seen possibilities of improvements by using a modified Gurson model which takes in to account the void growth at low triaxiality and shear dominated states and the need for a cell model using a kinematic material hardening.

Sammanfattning

Denna rapport syftar till att presentera arbetet som är utfört i projektet "Numerical simulation of ductile crack growth in residual stress fields". Arbetet omfattar ett experimentellt arbete samt numerisk mikromekanisk modellering av utförda experiment. Materialet som har använts i det experimentella arbetet är A533B-1.

Från de experimentellt framtagna J_R-kurvorna, kunde en stor effekt på brottsegheten utläsas för de provstavar som förbelastats till nivåer på 6% total töjning. Denna effekt kunde ses hos provstavar förbelastadade i både drag och tryck, dock kunde en större effekt på brottsegheten ses för provstavar förbelastade i drag. Vidare visade J_R-kurvorna att en förbelastaning till nivåer på 1.5 % och 3 % total töjning ej gav någon effekt på J_{Ic}. Notera att de effekter som observerats är på grund utav en förbelastning vid rumstemperatur, således är dessa resultat ej representativa exempelvis för de fall där material erhåller en nivå av plastisk förbelastning orsakad av svetsning.

Metodiken som beskrivs av Faleskog et al. [1] och Gao et al. [2] för att bestämma materialparametrarna till den mikromekaniska modellen, utifrån ett enaxligt dragprov samt ett brottmekaniskt standardprov, har i den numeriska delen av arbetet visats vara en strukturerad och tillförlitlig metod.
Mikromekanisk modellering med en cellmodell ger bra prediktioner av de experimentella J_R-kurvorna för förbelstningsnivåer upp till 3% i både drag och tryck. Men den mikromekaniska cellmodellen klarar ej att återge last-CMOD kurvorna och de stora effekterna på brottsegheten som ses för höga förbelastningsnivåer. Detta skulle sannolikt kunna åtgärdas av en mikromekanisk cell modell där ett kinematiskt hårdnande definieras för materialmodellen. Det numeriska arbetet visar vidare att den mikromekaniska cellmodellen klarar att prediktera effekterna av ett restspänningsfällt, som kunde observeras i tidigare experiment utförda av Bolinder et al. [3], på last-CMOD kurvor, på brottsegheten, och även återge det minskande inflytandet på J-integralen från restspänningarna för ökande primär last.
De med mikromekanisk cellmodellering predikterade J_R-kurvorna, för provstavar med och utan restspänningar, ligger på den övre avgränsningen för spridningen hos de experimentella resultaten. Detta innebär en mindre överskattning av brottsegheten. Denna överskattning kan åtgärdas med hjälp av en modifierad Gursonmodell som tar hänsyn till hålrumstillväxt vid låg spänningstreaxlighet och skjuvdominerat tillstånd.

Rapporten har visat på förmågan hos mikromekanisk cellmodellering att prediktera effekterna på duktil initiering och spricktillväxt från en begränsad förbelastning och ett restspänningsfällt. Dock har även möjligheter till förbättringar av prediktionerna belysts. Dessa förbättringar skull vara genomförbara med en modifierad Gursonmodell som tar hänsyn till hålrumstillväxt vid låg spänningstreaxlighet och skjuvdominerat tillstånd samt med möjligheten att definiera ett kinematiskt hårdnande hos materialmodellen.

Contents

Acknowledgement

The author is grateful for the financial support of the Swedish Radiation Safety Authority. This project was conducted in close collaboration with the department of Solid Mechanics at KTH, where the theoretical expertise received from Jonas Faleskog during the project and the experimental expertise from Hans Öberg and Martin Öberg are very much appreciated. The author would also like to thank AMEC UK for assisting in supplying the material used in the experiments.

1. Introduction

Cracked components are usually subjected to loads causing both primary and secondary stresses. The main contribution to secondary stresses is usually weld residual stresses. Engineering assessment methods such as the ASME XI code and the R6 procedure are commonly used to conduct assessments of such components. How these codes treat secondary stresses differ. ASME XI code does not consider secondary stresses in some materials while the R6 method on the other hand sometimes tends to give overly conservative assessments.

In Sweden the contribution from the secondary stresses and the primary stresses to K_I or J is treated equally important for components subjected to low primary loads i.e low L_r values. But for high primary loads (high L_r values) the contribution from the secondary stresses is weighted down according to the procedure developed by Dillström et al. in [4]. This treatment of secondary stresses has been verified experimentally by Bolinder et al. [3]. To experimentally examine the contribution of secondary stresses, in particular weld residual stresses, to K_I or J at low loads (low L_r values) is more complicated and practically difficult. Hence to be able to numerically simulate these kinds of experiments would be very beneficial. This could be possible with a model describing the micromechanical process for ductile tearing such as the Gurson model.

Earlier studies have already shown good predictions of JR-curves using micromechanical modeling with the Gurson model, studies have also determined the ability to account for constraint and size effects with the Gurson model, see the work done by Gao et al. [2] [5]. The ability for the Gurson model to handle load history and residual stresses still remains to be studied.

The goal for the work described in this report is to evaluate the ability of the Gurson model in predicting the effect from load history and residual stresses. This is a first and necessary step towards a future and final goal that would be to simulate ductile initiation and tearing in situations with high residual stresses. This could possibly give a basis to lower the contribution from the residual stresses to K_I or J at low primary loads (low L_r values), provided that the material behavior is ductile.

In this report, the project “Numerical simulation of ductile crack growth in residual stress fields” will be described. The report contains the theoretical background to ductile fracture and micromechanical modelling, the experimental program with a discussion of the results, the micromechanical modelling and resulting numerical predictions, a discussion of the numerical and experimental results, as well as conclusions drawn from the work.

2. Theoretical background

2.1. Fracture mechanics of ductile tearing

Ductile fracture in common structural and pressure vessel steels is characterized by the forming and coalescence of micro voids from impurities such as inclusions and second phase particles. As large plastic deformations on the micro level develop in front of the macro crack, voids nucleate from inclusions, as the load is increased the formed micro voids grow. Finally micro voids from second phase particles such as carbide inclusions coalescence and assist the tearing of the ligaments between the enlarged voids. This process creates a weakened band in front of the macro crack allowing an extension of the macro crack. These mechanics are driven by the combination of high triaxial stresses and high plastic strains ahead of the macro crack. Nucleation of voids typically occurs for particles at a distance of ~2δ (CTOD)[1] from the crack tip while the void growth occurs much closer to the crack tip relative to CTOD. In Figure 2.1 below the process of ductile crack growth is illustrated.

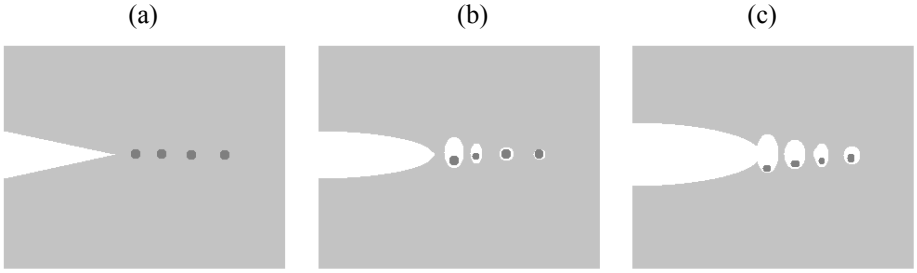

Figure 2.1. Mechanics of ductile crack growth, (a) Initial state, (b) Nucleation and growth of voids, (c) Coalescence of voids with macro crack

2.2. Micromechanical modeling of ductile tearing

With a cell model the growth and coalescence of voids and the interaction between the fracture process zone and the background material is modeled. By describing the ductile tearing with a cell model there is a possibility to study the influence of different parameters on ductile fracture.
With a cell model the material in the fracture process zone is modeled by an aggregate of similarly sized cells which form a material layer with the height D as illustrated in Figure 2.2.

[1] Crack Tip Opening Displacement

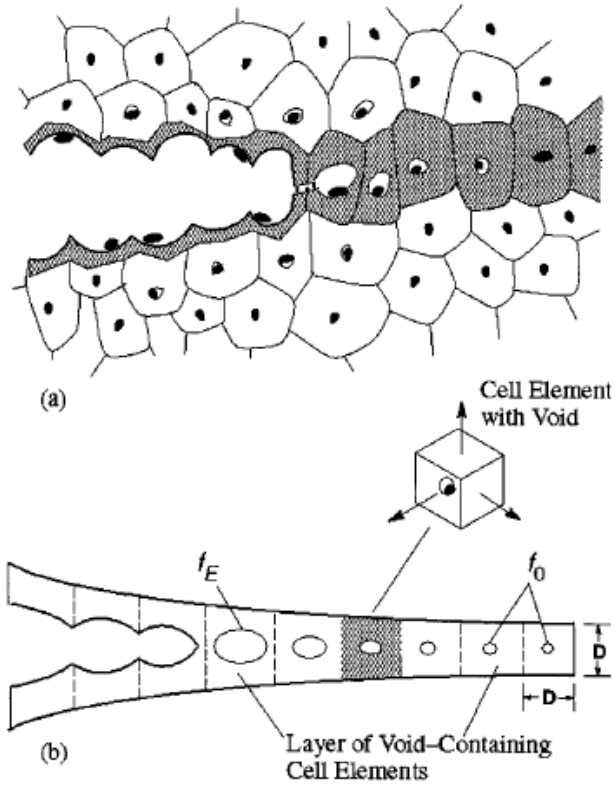

Figure 2.2. Illustration of cell modeling of ductile tearing.

The cell model approach was originally proposed by Xia and Shih [6] [7]. Each cell is a three dimensional element with dimension D comparable to the spacing between large inclusions. Each cell contains a spherical void of initial volume fraction f_0. The material outside the cell layer is modeled as standard elasto-plastic continuum. The damage mechanism in the cell layer, void growth and coalescence are modeled using Gurson's constituitive relation [8] with modification introduced by Tvegaard [9]. The Gurson model is a homogenized material model where spherical voids are treated in a smeared out fashion. The form of the yield condition $\Phi(\sigma_e,\sigma_h,\sigma_f,f)=0$ used in this report, which is incorporated in ABAQUS [10], applies to strain hardening materials with isotropic hardening as follows

$$\Phi = \frac{\sigma_e^2}{\sigma_f^2} + 2q_1 f \cosh\left(q_2 \frac{3\sigma_h}{2\sigma_f} \right) - 1 - q_1^2 f^2 = 0 \tag{1}$$

where f is the current void volume fraction , σ_e the macroscopic effective Mises stress, σ_h the macroscopic hydrostatic stress and σ_f the current matrix flow strength. The parameters q_1 and q_2 where introduced by Tvergaard [9] to improve model predictions.

Ductile crack growth occurs when a cell loses its stress carrying capacity by strain softening due to void growth that cannot be compensated for by material strain hardening. This process is not accurately captured by the Gurson model. Tvergaard and Needleman [11] therefore proposed to model this process as follows: When the void volume fraction f reaches a critical value of f_c the void growth is increased rapidly to the point when the void volume fraction reaches f_E at this point total

failure at the material point occur and once all the elements material points fail the element is rendered extinct. The parameters f_c and f_E are user specified. In ABAQUS this is modeled by the following function,

$$f = \begin{cases} f & \text{if } f \le f_c \\ f_c + \dfrac{\overline{f}_F - f_c}{f_E - f_c}(f - f_c) & \text{if } f_c < f < f_E \end{cases} \tag{2}$$

where

$$\overline{f}_F = \frac{1}{q_1} . \tag{3}$$

2.3. Determine cell model parameters

A scheme to determine the material parameters needed in the cell model is proposed by Faleskog et al. [1] and Gao et al. [2] and is summarized here. The parameters needed for the cell model are listed below:

Continuum Parameters:
- Elasticity: E, ν
- Plasticity: stress-strain relation

Cell model parameters:
- Micromechanics: q_1, q_2, f_E, f_c
- Fracture process: D, f_0

The continuum parameters can be determined by standard material testing. Due to the small stress triaxiality during a uniaxial tensile test, existing micro voids will not experience any significant void growth. Hence the measured uniaxial stress strain curve can be considered as representative for the behavior of the matrix material. The cell model parameters are decided in two steps, first the micro-mechanics parameters are decided and secondly the fracture process parameters.
The two parameters q_1 and q_2 in the Gurson model strongly depends on the yield strength and the strain hardening of the material. In [1] q_1 and q_2 values for various σ_0 and N are given hence the micro-mechanics parameters can be determined from a power hardening function describing the stress-strain curve of the material. The procedure to determine q_1 and q_2 is detailed by Faleskog et al. in [1].
The parameters f_c and f_E, controlling the extinction of the cell element, do not influence the J_R-curve in any significant way if they are chosen in the interval 0.10-0.20 see Figure 2.3 and Figure 2.4. Values of f_c lower than 0.10 does however influence the J_R-curve see Figure 2.4. Hence the model predictions are not sensitive to the choice of f_c and f_E as long as the chosen values are in the range 0.10-0.20.

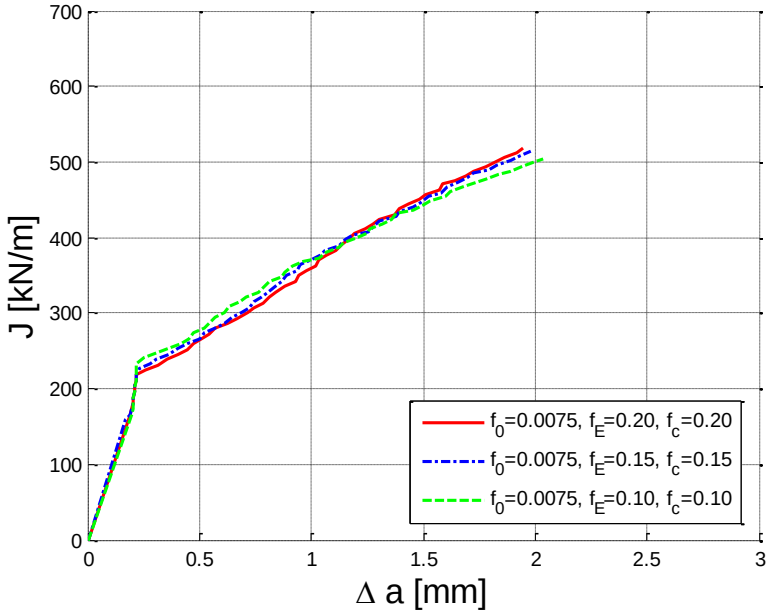

Figure 2.3. Comparison of numerical J_R-curves for models with varying f_E and f_c.

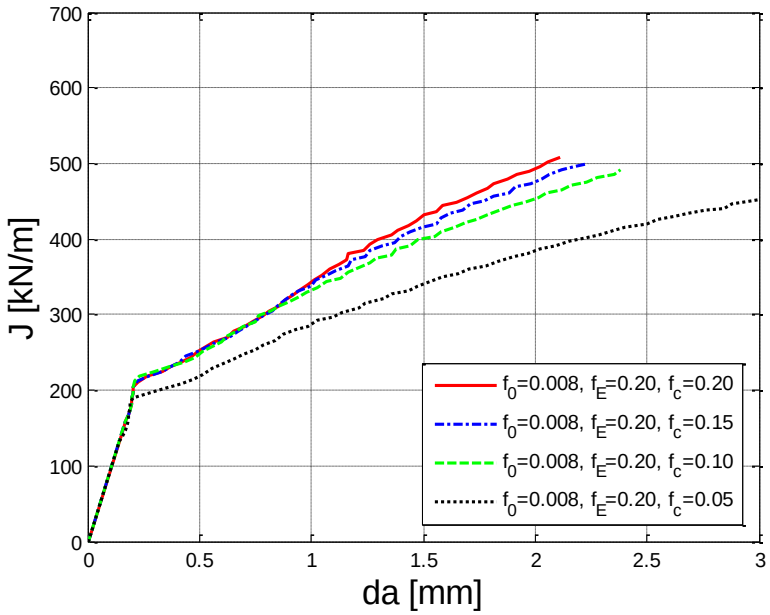

Figure 2.4. Comparison of numerical J_R-curves for models with varying f_c.

The second step is to determine the fracture process parameters. This procedure is described in more detail in [2]. The fracture process parameters f_0 and D are the main parameters controlling the crack growth resistance behavior. To successfully determine these parameters experimental data describing the crack growth behavior is needed. An experimentally generated J_R-curve is a suitable candidate for this purpose. D can be determined from the crack tip opening displacement (CTOD) at initiation. CTOD scales with the near tip deformation and is also a relevant measure of the size of the fracture process zone. To take D as the CTOD at initiation is

therefore suitable. CTOD at crack initiation or D can be determined from J_{Ic} with the relation

$$D \approx d \frac{J_{Ic}}{\sigma_y} \tag{4}$$

where J_{Ic} is the J-value at initiation of crack growth, σ_y is the yield strength and d is a non-dimensional constant ranging from 0.30 to 0.60 depending on the material strain hardening and yield strength [12]. Finally f_0 can be determined from matching the cell model to the experimentally generated J_R-curve. Below in Figure 2.5 the influence of f_0 on the J_R-curve is illustrated.

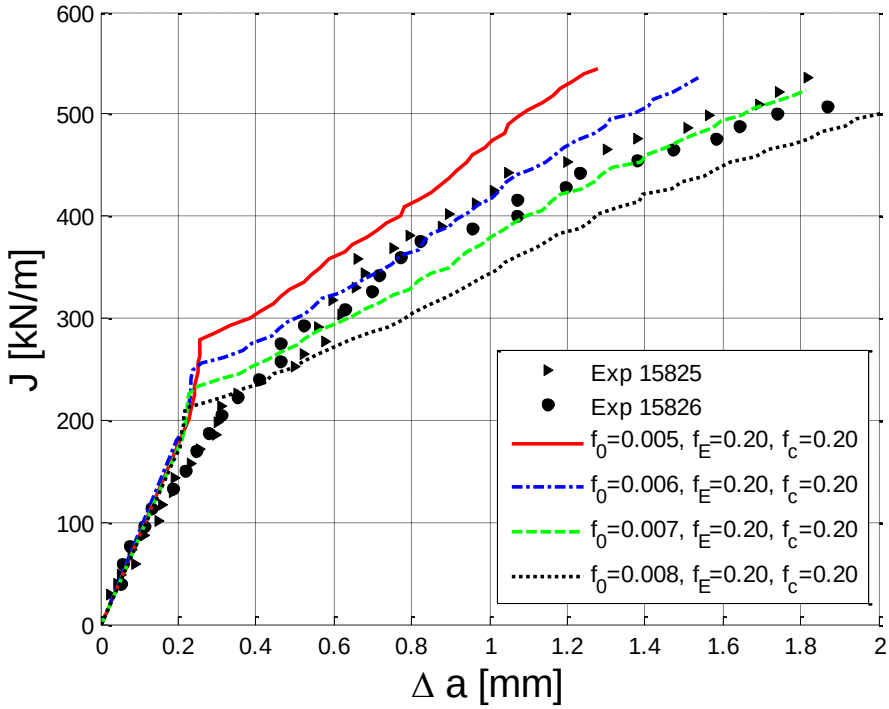

Figure 2.5. Effect of varying initial void volume fraction, f_0, on the J_R-curve, experimental results (Exp 15825, Exp 15826) presented in Chapter 3.

In order to generate a J_R-curve from the numerical results of the cell model the location of the crack front needs to be defined. In all analyses in this report the crack front is defined by the line connecting locations at the crack plane where f=0.1. At f=0.1 a cell element has lost most of its load carrying capacity. Furthermore the J-integral needs to be calculated. In this report two different procedures were used to calculate the J-integral. These are explained later in Chapter 5.

3. Experimental program

All the experiments were conducted at the department of Solid Mechanics at KTH. The background for the experiments was the need to look at the influence of load history on material fracture toughness. Earlier experiments by Bolinder et al. [3] have looked at the effect on the fracture toughness from residual stress fields. The residual stress fields were introduced by pre-loading the specimens. This raised the question what influence the pre-loading had on the material fracture toughness. Experiments were conducted representing the level of pre-loading the specimens were subjected to in [3]. These test showed no significant effect from the pre-loading on the material fracture toughness. However the question was still what effect pre-loading in tension and to higher levels of pre-load could have on the material fracture toughness. Therefore these new experiments were needed. This since it was important to examine if the numerical material model could handle the load history in a correct manner.

In the experimental program, it was decided to look at one material, the reactor pressure vessel steel A533B-1. This is the same material which had been used in [3], thus there was no need to perform any standard uniaxial tensile tests or cyclic tests, since these tests had already been conducted and the test data was available. In Figure 3.1 the stress-strain curve of the material A533B-1 is shown.

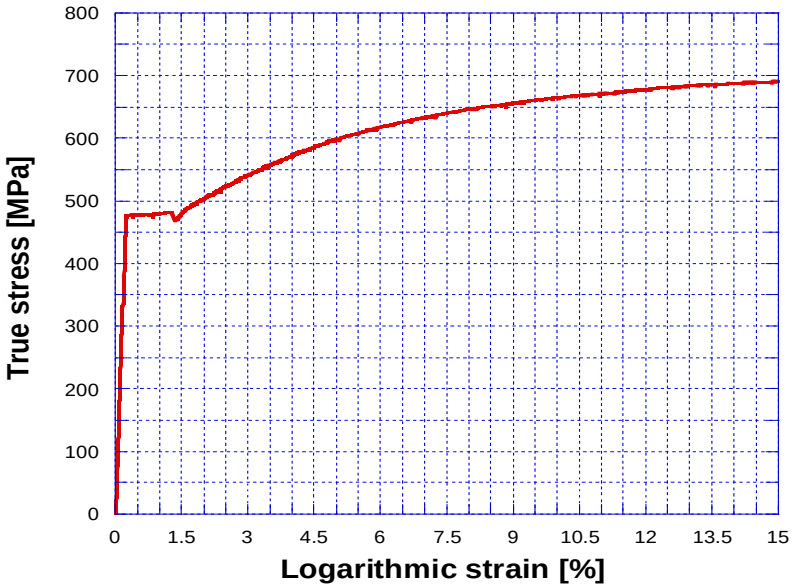

Figure 3.1. Stress-strain curve of material A533B-1 at room temperature.

To examine the effect of load history, specimens subjected to different levels of compression or tension were used. To look at the isolated effect of the load history, the pre-loading of the material was done so it would not introduce any residual stresses, this will be described below. After the materials had been pre-loaded, 3PB specimens with side groves were manufactured from the pre-loaded materials. These test specimens were then used in standard *J-R* tests to determine the J_{Ic} values. In Figure 3.2 the specimen geometry is shown. Below the test program is outlined.

- Material pre-loaded in compression, 6 specimens
  - Material: A533B-1
  - Level of pre-load: 1.5%, 3% and 6% total strain
  - Specimen Geometry: W= 27 mm, B=W/2, S=4W, a=0.5W
  - Testing: J-R tests in 3PB
- Material pre-loaded in tension, 6 specimens
  - Material: A533B-1
  - Level of pre-load: 1.5%, 3% and 6% total strain
  - Specimen Geometry: W= 27 mm, B=W/2, S=4W, a=0.5W
  - Testing: J-R tests in 3PB
- Material not pre-loaded, 2 specimens
  - Material: A533B-1
  - Level of pre-load: 0% total strain
  - Specimen Geometry: W= 27 mm, B=W/2, S=4W, a=0.5W
  - Testing: J-R tests in 3PB

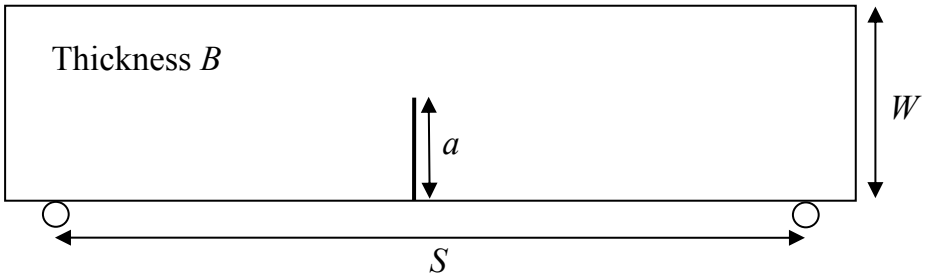

Figure 3.2. Base geometry of specimens.

3.1. Pre-Loading

Pre-loading of the material was conducted to three different levels of total strain both in tension and compression. For the material pre-loaded in compression, three rectangular pieces of the material were machined. These three pieces were then loaded at room temperature to a maximum total strain of 1.5%, 3.0% and 6.0%. From these rectangular loaded pieces the test specimens were then machined. In Figure 3.3 the dimension and the orientation of the test specimens can be seen.

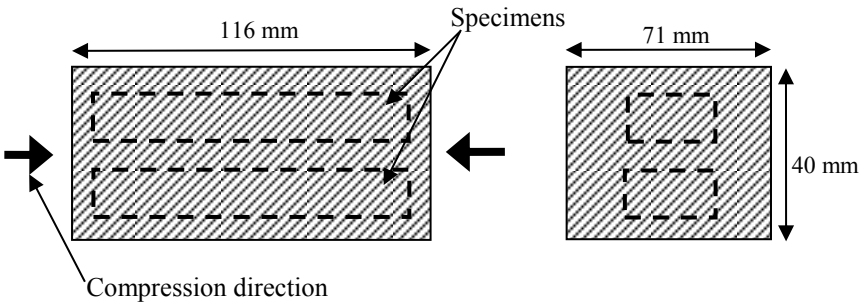

Figure 3.3. Dimensions of material pre-loaded in compression.

For the material pre-loaded in tension, cylindrical pieces of material were machined. These cylindrical rods were threaded in the end for mounting in the testing rig. These three pieces were then loaded in tension at room temperature to a maximum total strain of 1.5%, 3.0% and 6.0%. From each rod, two specimens were then machined, as can be seen in Figure 3.4.

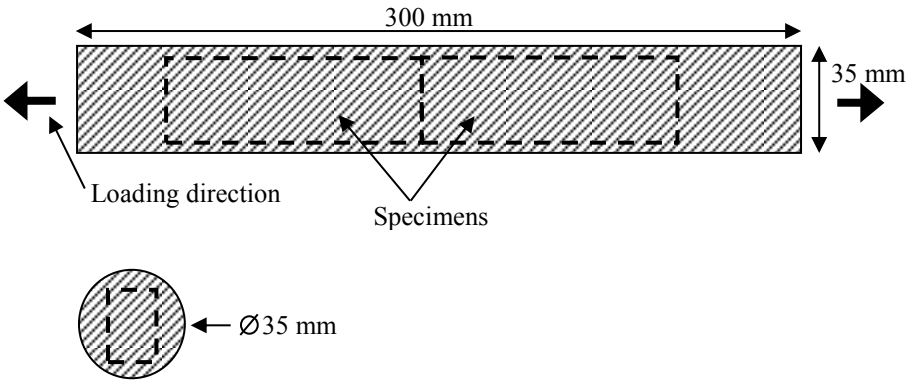

Figure 3.4. Dimensions of material pre-loaded in tension.

3.2. Fracture testing

The fracture tests were conducted as standard *J-R* testing according to ASTM E 1820 [13]. All specimens were loaded in 3PB during the fracture testing. The load, CMOD and LLD (Load Line Displacement) data were recorded during the tests. The crack growth was monitored with compliance calculations. The tests were ended with a fatigue loading in order to obtain two different crack fronts on the crack surface. The first front is the initial crack depth and the second is the fatigue front at the end of the testing. After the fracture testing was finished, the specimen was broken up to show the crack surfaces, and also to measure the different crack fronts.

4. Experimental results and discussion

Below in Figure 4.1 the load-CMOD (Crack Mouth Opening Displacement) curves of the performed tests are shown. The curves are shown without the unloadings for clarity. All the curves for the respective specimens are presented in Appendix A with unloadings for the compliance measurements. For Figure 4.1 the red color corresponds to a pre-load of 6% total strain, green color corresponds to 3% total strain, blue color correspond to 1.5% total strain and black corresponds to no pre-load.

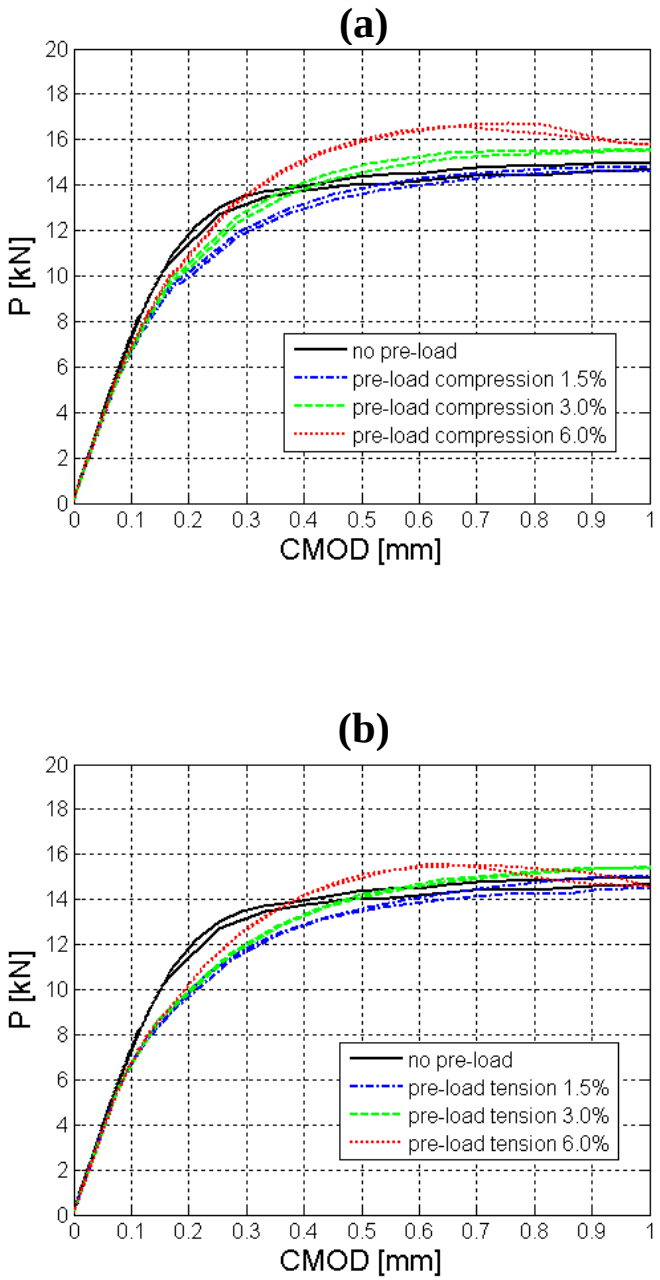

Figure 4.1. Experimental load-CMOD curves for (a) specimens pre-loaded in compression, (b) specimens pre-loaded in tension.

From the load-CMOD curves, a clear effect of the pre-loading of the material can be seen for all levels of pre-load. The load-CMOD curves indicate hardening of the material for 3.0% and 6.0% pre-load but not for 1.5 %. These are reasonable results, considering the stress-strain curve of the material seen in Figure 3.1. In Figure 3.1 it can be seen that the material has a large Lüder strain region up to approximately 1.5 % logarithmic strain. The results also indicate that the pre-loaded specimens start to plastically deform earlier than the virgin material. One explanation to the trend seen in Figure 4.1 is the Bauschinger effect. The global moment gives rise to both compressive and tensile stresses over the ligament of the specimen. In the case where the specimens were pre-loaded in compression, the tensile part of the stresses over the ligament will lead to earlier plasticity than what would be the case for a virgin material and vice versa for the material pre-loaded in tension. This can also be understood by the hysteresis loop from a cyclic test of the material seen below in Figure 4.2. The reversed stresses in regards to the pre-load will give rise to plasticity at a lower magnitude of stress. From the hysteresis loop from a cyclic test in Figure 4.2 it is evident that the material experiences the Bauschinger effect.

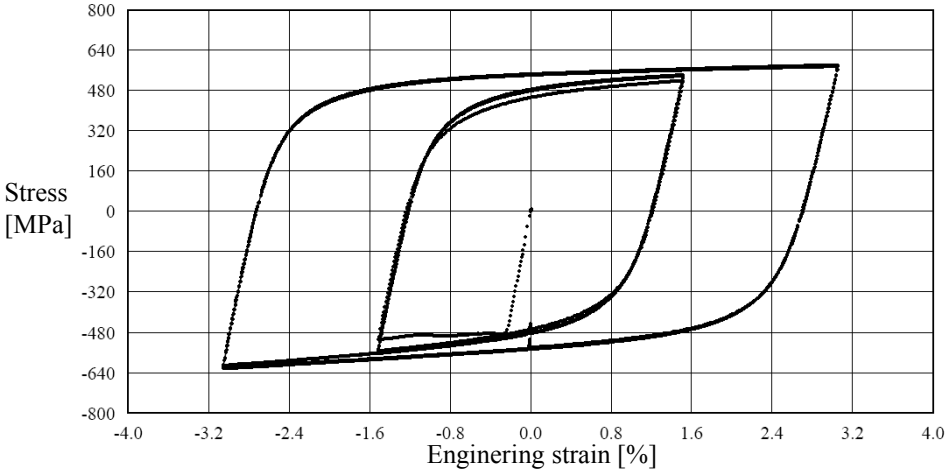

Figure 4.2. Cyclic test data for A533B-1.

The *J-R* test results from all the tests are presented below in Figure 4.3, Figure 4.4 and Table 4.1. All the individual J_R-curves are also presented in Appendix B. Figure 4.3 shows all the results for specimens pre-loaded in compression and no pre-load while Figure 4.4 shows results for specimens pre-loaded in tension and no pre-load. For both Figure 4.3 and Figure 4.4 the red color corresponds to a pre-load of 6% total strain, green color corresponds to 3% total strain, blue color correspond to 1.5% total strain and black corresponds to no pre-load.

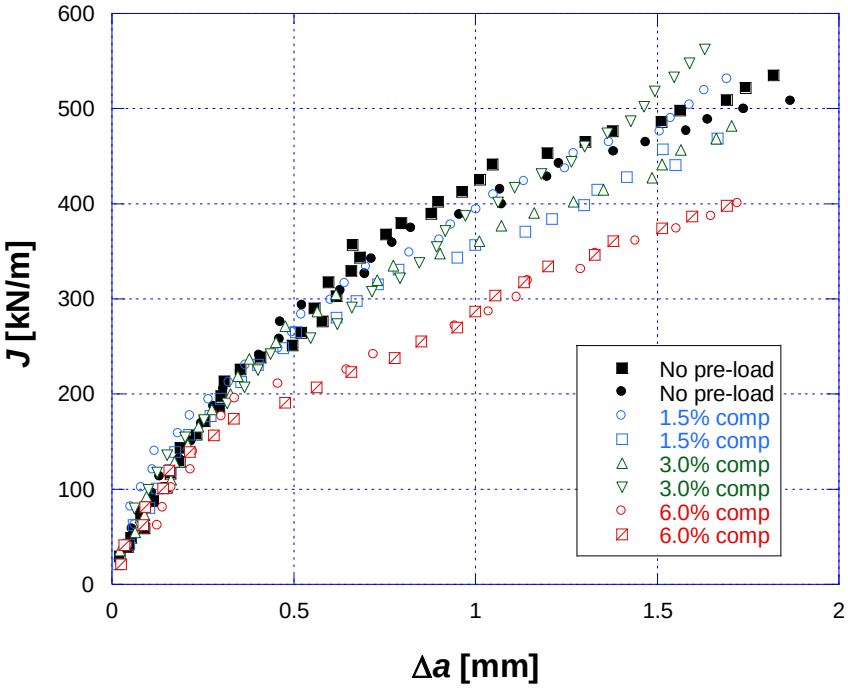

Figure 4.3. *J*-integral results versus crack growth, with and without compressive pre-load.

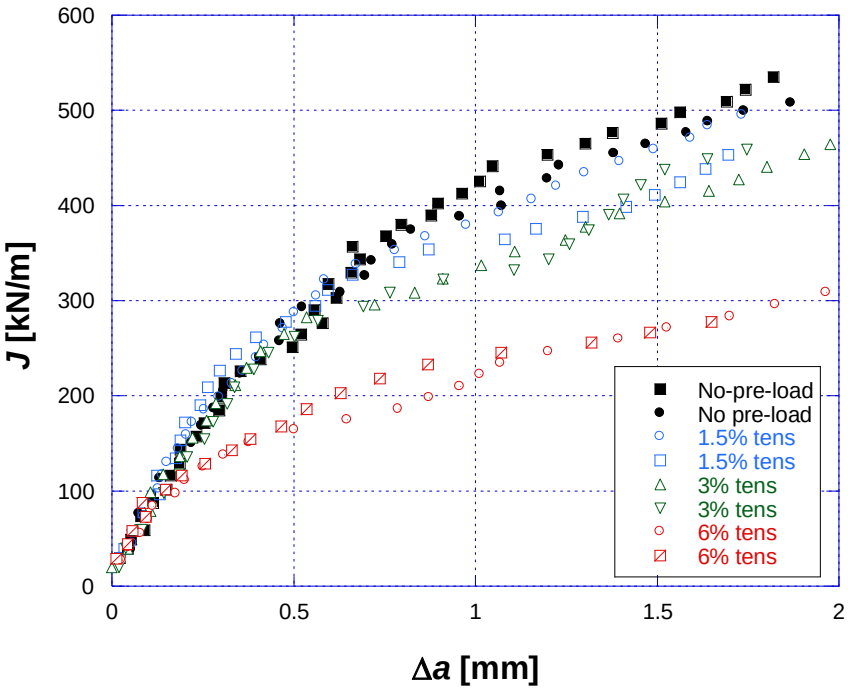

Figure 4.4. *J*-integral results versus crack growth, with and without tensile pre-load.

Table 4.1. J_{Ic} values for all the test specimens.

Total strain [%]	J_{Ic} for specimens pre-loaded in compression [kN/m]		J_{Ic} for specimens pre-loaded in tension [kN/m]	
0	249	262	249	262
1.5	249	235	270	279
3.0	256	220	248	238
6.0	170	163	137	152

From the results above, it is clear that for specimens pre-loaded to 6% of total strain a large effect from the pre-loading of the material is seen. This is true for both pre-loading in tension and compression but the effect is larger in the specimens pre-loaded in tension. It can also be concluded that no distinctive influence on crack initiation is observed from pre-loadings to 1.5 or 3 % total strain. There seem to be some kind of threshold value of pre-loading when the material toughness is altered see Figure 4.5. This threshold is apparently somewhere between 3% and 6%. The reason for the large difference in the observed change in material fracture toughness from a pre-load of 6% and not 1.5% or 3% total strain is not entirely understood yet. Earlier experimental work by Sivaprasad et al. [14] on HSLA (High Strength Low Alloy) steels have shown similar trends. Their results showed that for pre-loads up to 2 % no effect on the fracture toughness was seen. At greater pre-load levels their results showed a decrease in fracture toughness in almost direct proportion to the amount of pre-load. Experimental results on 316 stainless steel and 4340 steel presented by Liaw and Landes [15] did show on a decrease in fracture toughness regardless of the level of pre-load.

The experimental results presented in this report show furthermore a clear difference in the tearing resistance between specimens pre-loaded in compression and tension to 6%. This difference could be as a result of the forming and growth of micro voids during the tensile pre-load, leading to a weakening of the material. This could explain the seen difference in results between compressive and tensile pre-load. The results nevertheless point on a difference indicating a possible additional or lack of weakening mechanic during the pre-load.

It should be noted that the effects seen as a result of work hardening are due to a prior pre-load at room temperature. Hence these effects are not representable for cases were the material exhibits a level of plastic pre-strain caused by welding.

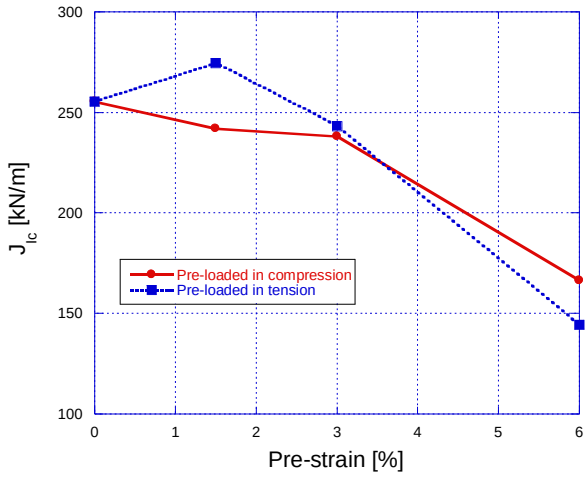

Figure 4.5. Effect from pre-load on material initiation fracture toughness.

5. Predictions using cell modeling

In this chapter predictions of experimental results described above in Chapter 4 and in [3], will be done by the use of micromechanical modeling. This can be done by the use of a cell model. With a cell model the growth and coalescence of voids and the interaction between the fracture process zone and the background material is modeled. The cell model parameters will be determined from experimental results of a standard 3PB specimen and a material stress-strain curve. Subsequently the cell modeling technique will be used with the determined material parameters in predicting the experimental results. The predictions will show the capability of the cell modeling technic employed in describing the effects from a prior pre-load or residual stress field. The numerical computations with the finite element method were executed with ABAQUS [10].

In order to generate J_R-curves from the numerical results of the cell models the *J*-integral needed to be calculated. Two different methods for calculating the *J*-integral were used. The reason for using two methods was that the standard method according to ASTM E 1820 [13] was not considered to give reliable data at low load levels for the specimens with residual stresses described in [3], since it does not take into account the elastic contribution from the residual stresses to the *J*-integral. An alternative method using FE-analyses was previously developed by Bolinder et al. in [3], for the nonstandard specimens with and without residual stresses. This method was also used in this report for evaluating the *J*-integral from the numerical results of the cell model. In the method a correlation between the *J*-integral and CMOD is obtained with the help of several FE-models. With this correlation the *J*-integral is obtained from the CMOD results, in Figure 5.1 an example of the *J*-CMOD curves is shown. For a thorough description of the method the reader is referred to [3]. The reason for using this method in evaluating the *J*-integral from the numerical results is to give an accurate comparison with the experimental results in [3]. The second method used in this report for evaluating the *J*-integral was the method described by ASTM E 1820 [13], the same method used for the experimental results in Chapter 3. With the exception, that the compliance is calculated from the average crack depth of the model instead of from loading and unloading of the model.

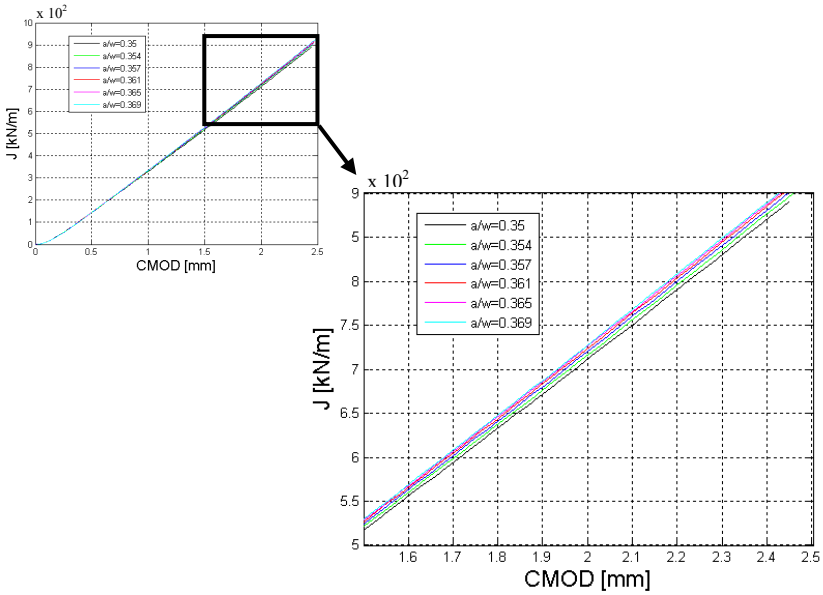

Figure 5.1. Example of *J-CMOD* curves used in evaluating the *J*-integral from the experiments.

5.1. FE-model

A python script was written in order to create a parameterized FE-model for ABAQUS. With this script it is possible to create a 3PB specimen with and without side grows and also with and without a notch. The geometries of the test specimens are given in Figure 5.2 with W=27 mm.

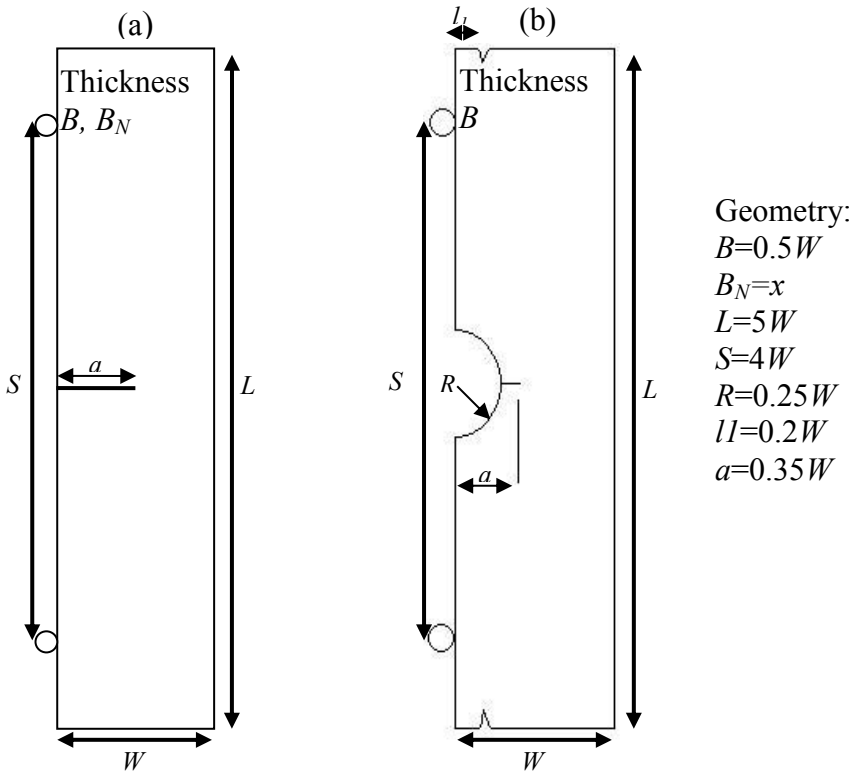

Figure 5.2. Base geometry of (a) standard 3PB specimen with side-grooves and (b) notched test specimen [3].

With the script it is possible to control the cell element layer in great detail. During the course of the work several FE-models were created with different setups of the element mesh. These were used in sensitivity analyses which led to the final element mesh setup described below. Due to symmetry, only a quarter of the models were modeled. In Figure 5.3 the two different FE-models used in the following analyses are shown.

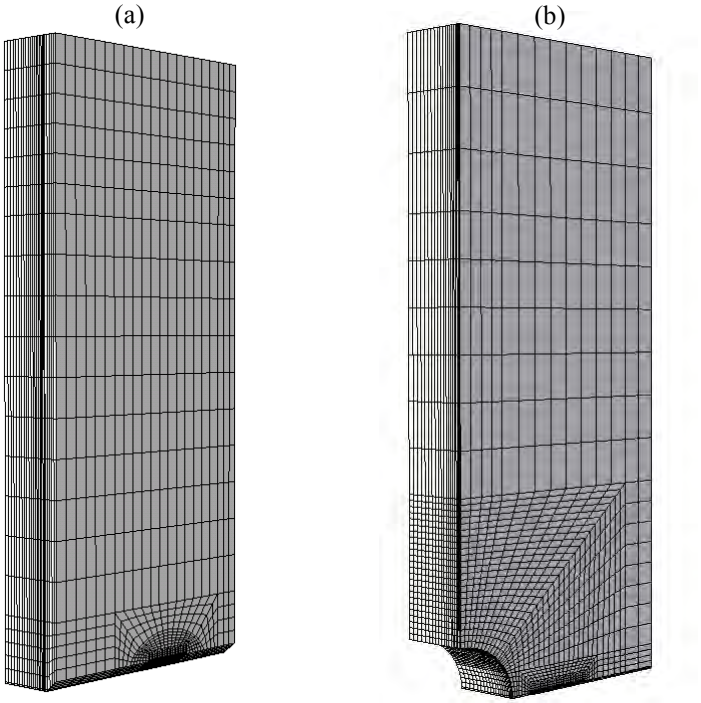

Figure 5.3. Three dimensional finite element mesh for (a) a quarter model of the side-grooved three point bending specimen, (b) a quarter model of the un-grooved notched three point bending specimen.

The fracture process zone or the cell element layer is shown in Figure 5.4. The cell elements were modeled with the height and length of D/2.

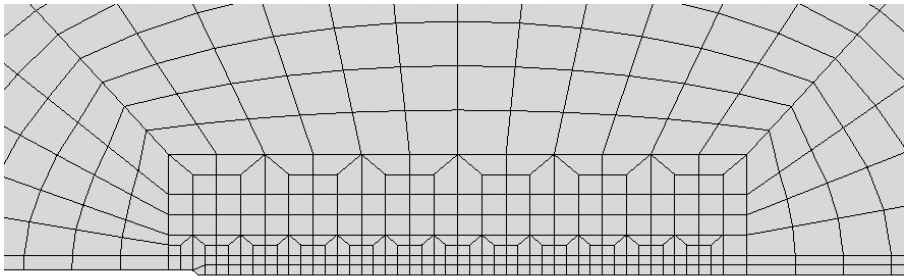

Figure 5.4. The arrangement of the void containing cells and the surrounding region.

The depth of the cell elements were varied with the position relative to the free surface with larger element depths near the center symmetry surface and smaller near the free surface. At the free surface the element depth was equal to *D*/2. Both FE-model were modeled with a total of 20 element layers through the thickness. In Figure 5.5 the element mesh trough the thickness is shown. A thorough study of the influence of element thickness is presented by Qian in [16]. This study was decisive in deciding the element layer set up. Both models used in the analyses were modeled with 8-node linear brick element with reduced integration and hourglass control (C3D8R).

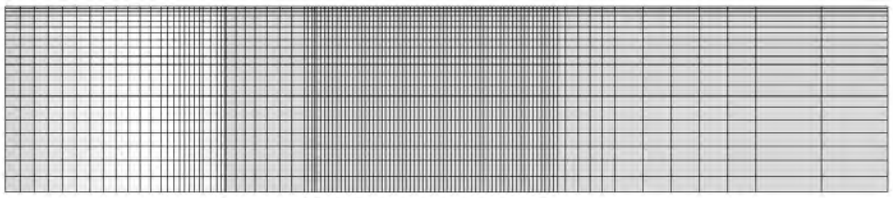

Figure 5.5. The arrangement of the finite element meshes through the thickness used in both FE-models.

5.2. Determining the cell model parameters

The matrix material behavior of the material model was modeled as elastic multilinear plastic with isotropic hardening. Using only isotropic hardening is a limitation imposed by using the material model incorporated in ABAQUS [10]. The material parameters for the matrix material are given below in Table 5.1.

Table 5.1. Matrix material parameters used in the FE-model for material A533B.

E = 205.3 GPa	ν= 0.3
σ [MPa]	ε^{pl}
471.2	0.0
480.3	0.010767
489.0	0.014855
507.6	0.018494
539.4	0.026489
576.0	0.038381
601.1	0.049059
621.4	0.060270
643.9	0.077280
657.7	0.091113
669.0	0.10652
683.6	0.13425
721.0	0.24436
809.0	0.44844

The micromechanical parameters q_1 and q_2 strongly depend on the material stress-strain relation. For this report q_1 and q_2 were decided from the correlations to σ_0 and N derived by Faleskog et al. in [1]. To be able to decide the parameters q_1 and q_2 the uniaxial tensile test result was fitted to a power law curve on the form,

$$\varepsilon = \frac{\sigma_0}{E} \qquad \sigma < \sigma_0$$
$$\varepsilon = \frac{\sigma_0}{E}\left(\frac{\sigma}{\sigma_0}\right)^{1/N} \qquad \sigma > \sigma_0. \tag{5}$$

Below in Figure 5.6 the stress-strain curve and the power law fit are shown.

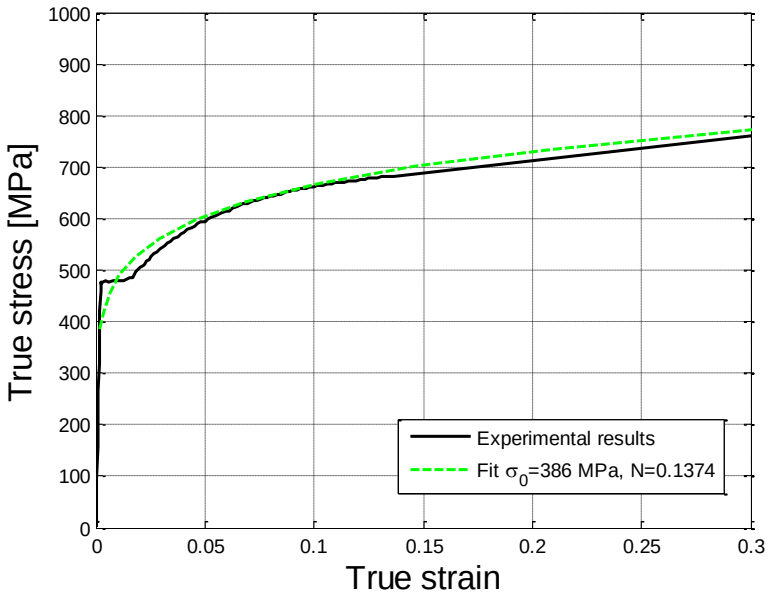

Figure 5.6. Stress-strain curve with power law fit for material A533B-1.

The values of the void volume fractions f_c and f_E is typically chosen in the interval 0.10 to 0.20. The model predictions are rather insensitive to the choice of f_c and f_E as long as the values are in the interval mentioned above. The results in Figure 2.4 show a slightly more curved J_R-curve for values of f_c and f_E set to 0.10 and 0.20 respectively compared to values of f_c and f_E both set to 0.20. This was considered when choosing values of f_c and f_E. In the following models f_c and f_E where set to 0.10 and 0.20 respectively. Below in Table 5.2 the micromechanics parameters used in the models in this report are presented.

Table 5.2. Micromechanics parameters used in the material model.

Micromechanics	
q_1	1.64
q_2	0.87
f_E	0.20
f_c	0.10

The fracture process parameters f_0 and D are the parameters primarily controlling the crack growth resistance behavior. These are hence decided from an experimentally determined J_r-curve. From the J_r-curve in Figure 5.7 the J_{Ic} value was determined which led to a D of 0.250 mm by the use of Equation 4.

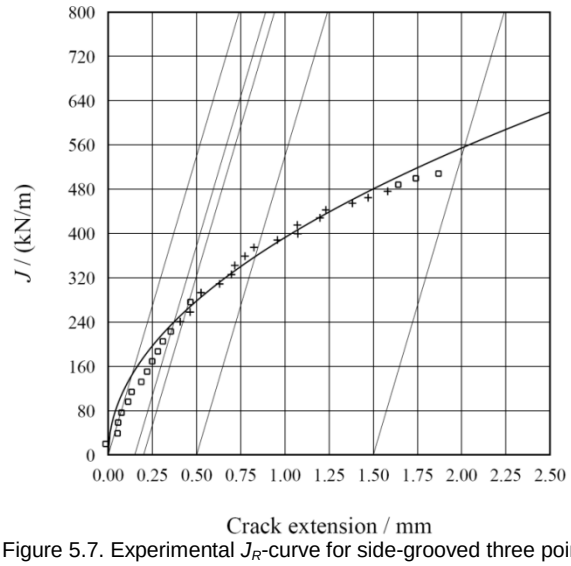

Figure 5.7. Experimental J_R-curve for side-grooved three point bend specimen without any prior preload.

The initial porosity f_0 was decided by matching the cell model predictions to the experimental J_R-curve see Figure 5.8. A f_0=0.0065 was chosen from these results.

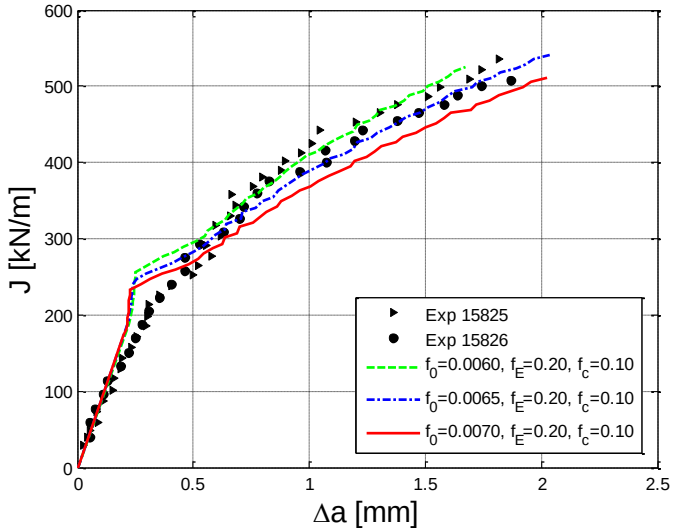

Figure 5.8. Predicted J_R -curves with varying f_0 compared with the experimental data for side-grooved three point bend specimen without any prior preload.

In **Table 5.3** the fracture process parameters used in ABAQUS [10] for the material model are presented.

Table 5.3. Fracture process parameters used in the material model.

Fracture process	
D [mm]	0.250
f_0	0.0065

In Figure 5.9 the load-CMOD curve from the experiment is compared with the results from the FE-model, as can be seen the comparison shows a good agreement between the FE-model and the experimental results. The predicted crack front from the FE-model is also compared to the experimental measurements see Figure 5.10. From the comparison Figure 5.10 it can be seen that the FE-model gives a good prediction of the crack front with the exception of near the free surface. This is due to the low triaxiality at the free surface. The Gurson material model underestimates the void growth at low stress triaxiality. This can be rectified by using the modified Gurson model which takes in to account the void growth at low triaxiality and for shear dominated states.

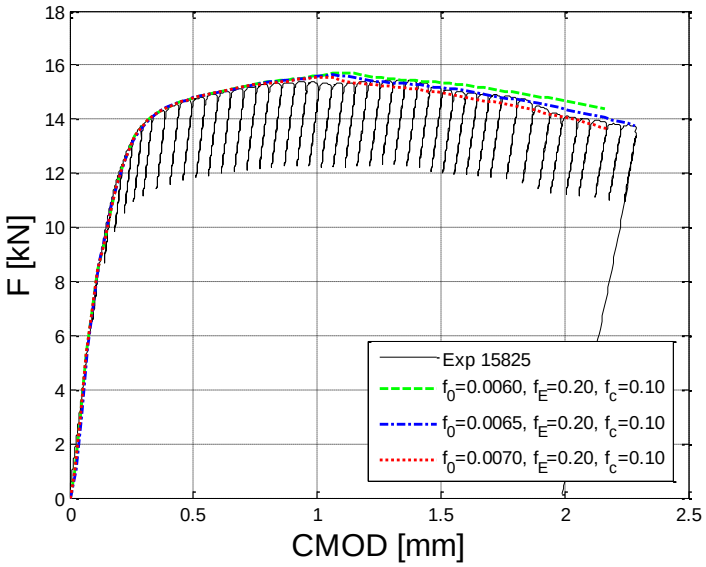

Figure 5.9. Predicted load-CMOD curves with varying f_0 compared with the experimental load-CMOD curve for side-grooved three point bend specimen without any prior preload.

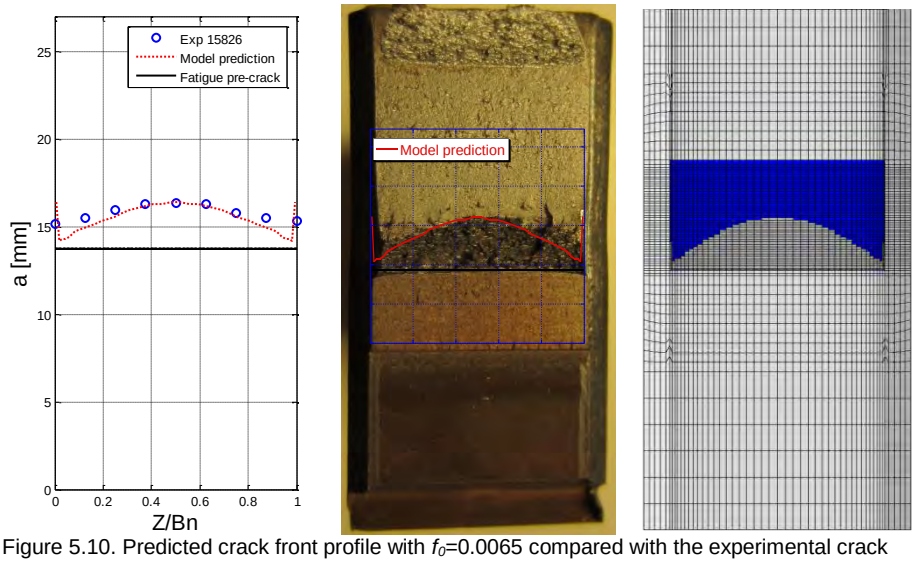

Figure 5.10. Predicted crack front profile with f_0=0.0065 compared with the experimental crack front profile for side-grooved three point bend specimen without any prior preload.

5.3. Evaluation of the capability of the cell modeling technic in capturing the effects of a prior pre-load on fracture toughness

To predict the effects from the load history with the cell model, the effect on the material characteristics need to be accurately modeled. These effects need to be incorporated in the model. The effects on the material due to the pre-load are work hardening and possible void volume growth for the specimens loaded in tension. To simulate the work hardening effects in the cell model a hardening initial condition was set. There is however a limitation in the Gurson material model incorporated in ABAQUS. It is only possible to simulate isotropic hardening behavior using the inbuilt Gurson material model in ABAQUS. Hence the Bauschinger effect cannot be modeled. As can be seen from the Figure 4.2 the material used in the experimental work exhibits a clear kinematic hardening behavior. This will possibly lead to problems in correctly capturing the seen effect at large pre-load levels. Below a study of the possibility to correctly simulate the fracture behavior after a specific amount of pre-load in either tension or compression is presented.

5.3.1. Effect on material stress-strain curve and possible void volume growth

To determine the extent of work hardening and the possible void volume growth the material exhibits at different amount of pre-load a simple 1 element FE-model was used. The same material parameters determined in Chapter 5.2 were used for the model. In Table 5.4 the possible void volume growth and equivalent plastic strain are given for different levels of pre-load. These values were then used in the following analyses in determining the possibility to model the effect on the ductile fracture behavior from a pre-load at room temperature. For pre-load in compression it was argued that no void volume growth occurs.

Table 5.4. Equivalent plastic strain and void volume growth due to different levels of pre-load.

Pre-Load Total strain [%]	*Equivalent plastic strain*	*Void volume growth for f_0=0.0065*
1.5	0.0126	0.0000791
3.0	0.0275	0.000172
6.0	0.0567	0.000364

5.3.2. Numerical prediction of the effect from strain hardening

The different levels of strain hardening were applied to the model with the method of prescribing initial condition with type hardening in ABAQUS [7]. With this method the equivalent plastic strain is prescribed to the model to represent a prior pre-load. There is also a possibility to supply a backstress tensor but this is only relevant for kinematic material models and since the material is modeled with isotropic hardening the backstress is not relevant. Below in Figure 5.11 the predicted J_R-curves are compared to the experimental data for specimens pre-loaded in compression. In Figure 5.11 the red color corresponds to a pre-load of 6% total strain, green color corresponds to 3% total strain, blue color correspond to 1.5%

total strain and black corresponds to no pre-load. The comparison is made to the specimens pre-loaded in compression since no void growth occurs during the compressive pre-load. For the predicted results it is seen that the pre-load level do not give any significant effect on crack initiation, but a limited effect on the tearing resistance for pre-load levels of 3% and 6%. The comparison indicates that the cell model gives good prediction of the J_R-curve for pre-load levels up to 3%. As for the experimental results, no significant effect from the pre-load on the fracture resistance is seen for pre-load levels up to 3%. This indicates that a work hardening up to 0.0275 equivalent plastic strain do not influence the material fracture resistance in any significant way. From the comparison it is however clear that there is a problem to recreate the large effect seen at high pre-load levels of 6 %. Here the predicted results overestimate the material fracture behavior. The seen effect from the experimental results at a pre-load level of 6% is much larger than the predicted effect.

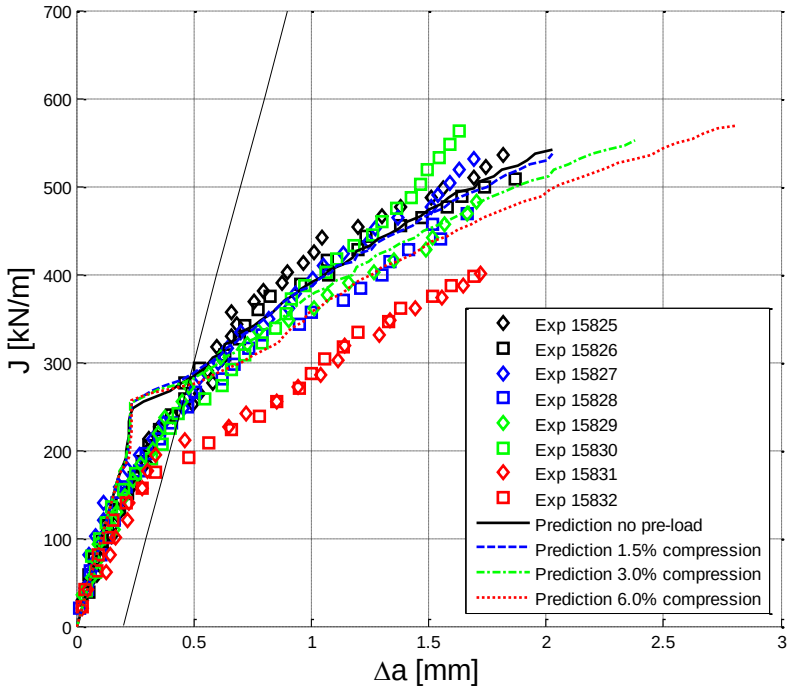

Figure 5.11. Predicted J_R -curves with varying pre-load level without additional initial void volume compared with the experimental data for side-grooved three point bend specimens with varying compressive pre-load levels.

If the load-CMOD curves are compared see Figure 5.12, it is seen that there are big differences between the predictions and the actual experimental results. These differences are larger for higher pre-load levels. The reason for these differences is the fact that the material is modeled with isotropic hardening while the material exhibits a strong kinematic behavior. To be able to accurately predict the effect from the pre-load on the load-CMOD results for this material, there is a need to use kinematic hardening. The isotropic hardening is not able to accurately capture the hardening behavior of the material. With the limitation of only using isotropic hardening with the inbuilt Gurson model in ABAQUS, a user subroutine describing the Gurson material model with kinematic hardening is needed to be successful in capturing the effects.

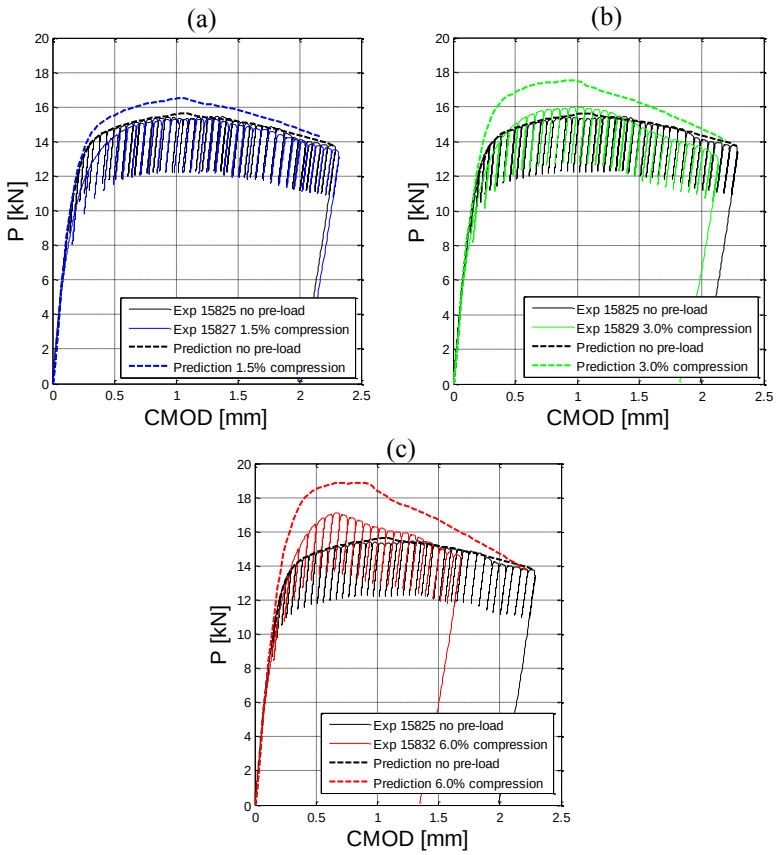

Figure 5.12. Predicted load-CMOD curves with varying pre-load levels compared with the experimental load-CMOD curves for side-grooved three point bend specimen with varying compressive pre-load level, (a) 1.5% total strain, (b) 3.0 % total strain and (c) 6.0% total strain.

5.3.3. Numerical prediction of the effect from void volume growth coupled with strain hardening

The effect of void volume growth for the specimens pre-loaded in tension is evaluated in this chapter. To evaluate the effect from void volume growth the initial void volume fraction f_0 was increased by the void volume fraction growth computed in Chapter 5.3.1 and presented in Table 5.4. The strain hardening was also added to the model as described in Chapter 5.3.2 above. The predictions were then compared with the experimental results from specimens pre-loaded in tension Figure 5.13. In Figure 5.13 the red color corresponds to a pre-load of 6% total strain, green color corresponds to 3% total strain, blue color correspond to 1.5% total strain and black corresponds to no pre-load. For the predicted results it is seen that there is no significant effect on crack initiation, but a limited effect on the tearing resistance for a pre-load level of 3% and a more distinct effect on the tearing resistance for a pre-load level of 6%. As for the results presented in Chapter 5.3.2 the predictions correlate with the experimental results at pre-load levels of 1.5% and 3%. At a pre-load level of 6% though, there is a big difference between the predicted results and the experimental results.

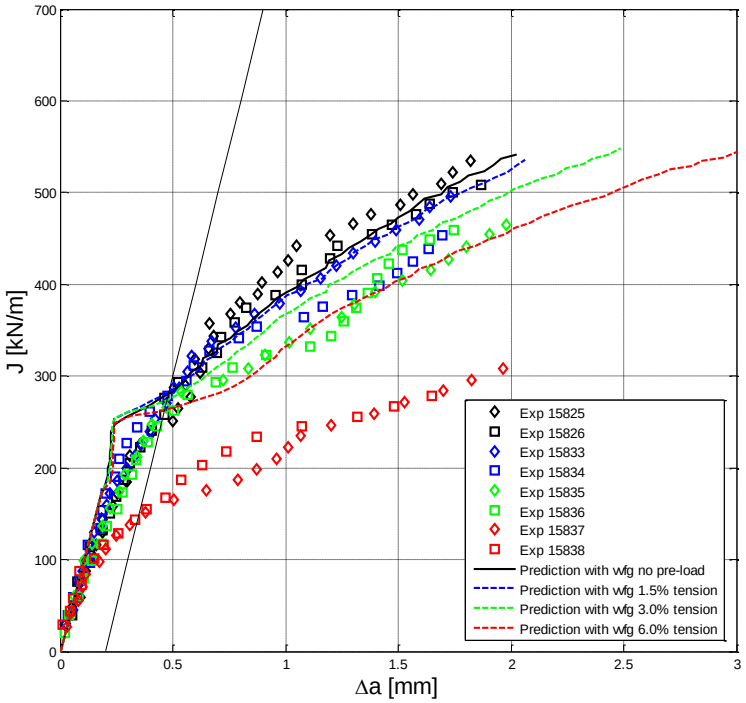

Figure 5.13. Predicted J_R -curves with varying pre-load level with additional initial void volume compared with the experimental data for side-grooved three point bend specimens with varying tensile pre-load levels.

In Figure 5.14 the effect from a void volume fraction growth is also illustrated by comparing to the prediction without applied void volume fraction growth. From these results it is evident that at a pre-load level of 1.5% the effect on the crack growth resistance is insignificant but as the pre-load level increases up to 6% the seen effect is substantially increased. This is a trend that also can be seen in the difference between the experimental results pre-loaded in compression and tension. The result show on lower fracture toughness for specimens loaded in tension at high pre-load levels compared with specimens loaded in compression. The specimens loaded at a pre-load level of 1.5 % do not show any significant difference between the specimens loaded in compression compared with the specimens loaded in tension. Hence the seen effect in the experimental results could be a result of the forming and growth of micro voids at high tensile pre-loads. The material does not experience this for a compressive pre-load or a low tensile pre-load.

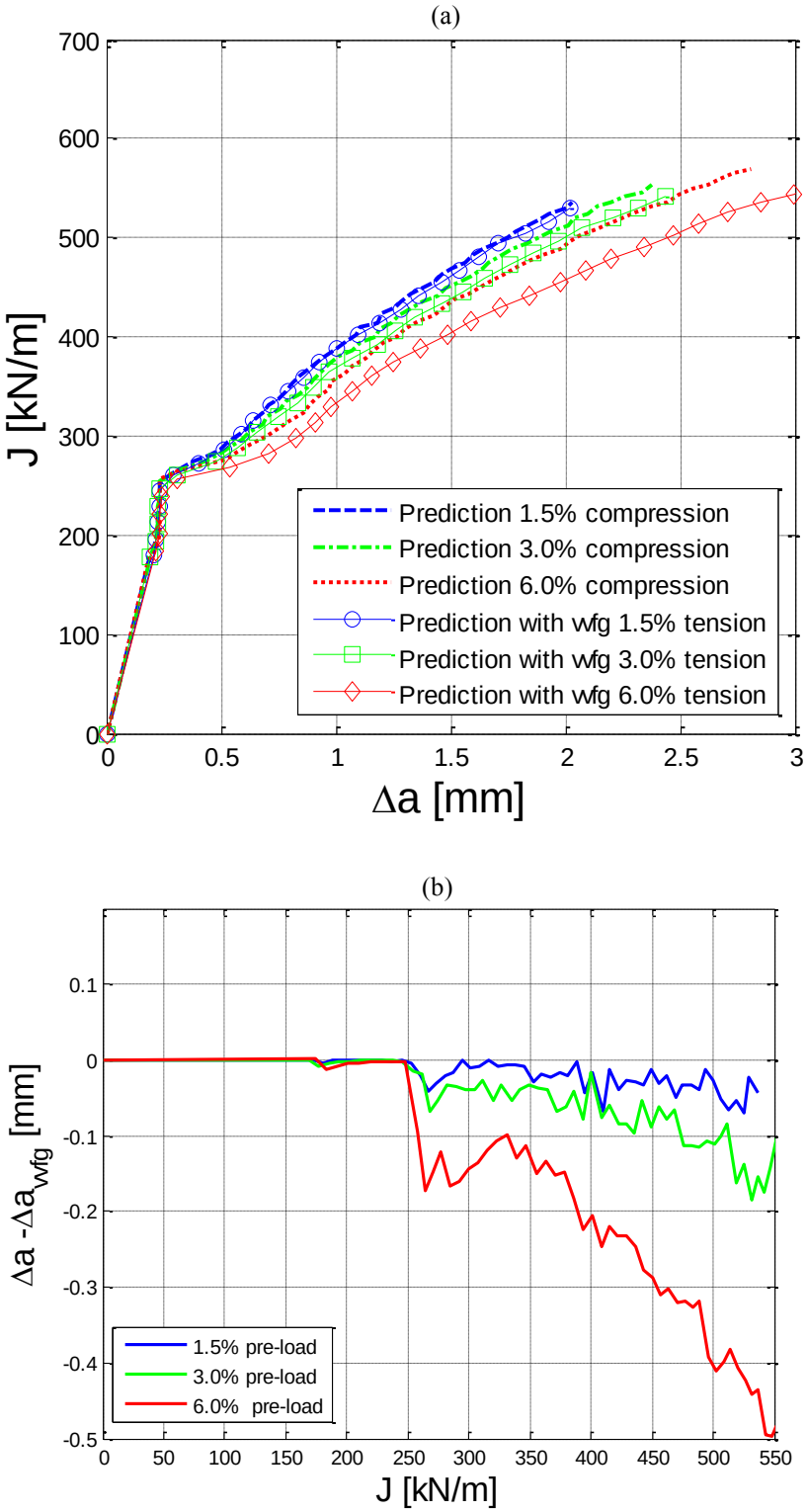

Figure 5.14. Comparison of (a) predicted J_R -curves with and without additional initial void volume, (b) difference in crack growth between models with and without additional initial void volume as a function of J.

In Figure 5.15 the load-CMOD curves are compared between the predicted results and the specimens pre-loaded in tension. As for the specimens pre-loaded in compression big differences between the predictions and the actual experimental results are observed. These differences are larger for higher pre-load levels. The reason for these differences is the fact that the material is modeled with isotropic hardening while the material exhibits a strong kinematic behavior.

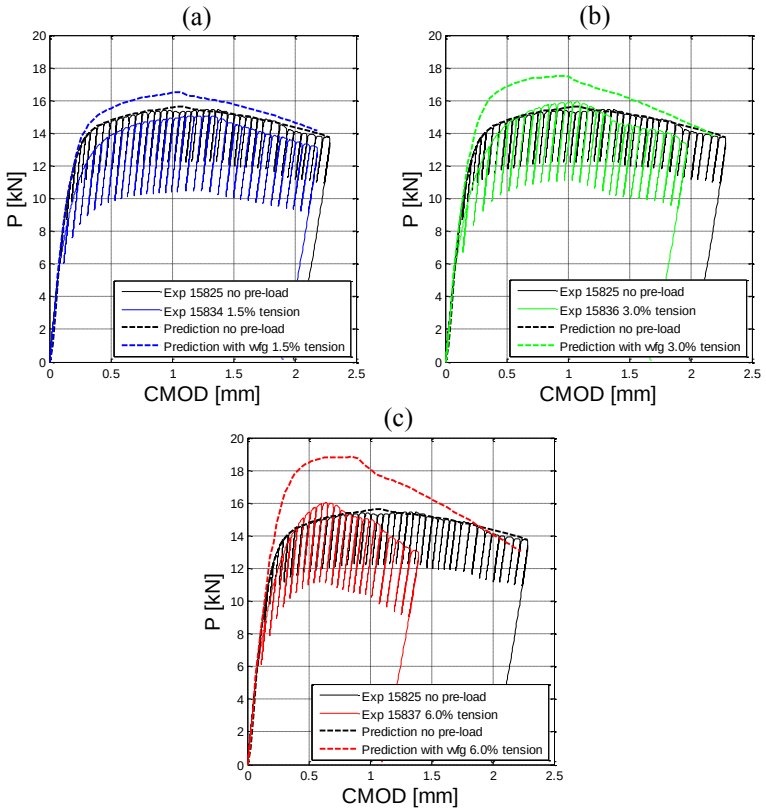

Figure 5.15. Predicted load-CMOD curves with varying pre-load levels compared with the experimental load-CMOD curves for side-grooved three point bend specimen with varying tensile pre-load level, (a) 1.5% total strain, (b) 3.0 % total strain and (c) 6.0% total strain.

5.4. Evaluation of the capability of the cell modeling technic in capturing the effects of residual stresses

In this chapter the capability of the cell modeling technique in capturing the effects of residual stresses will be evaluated. The ability to capture the effect of constraint will also be shown since the specimens used in [3] had a nonstandard geometry with a shallow crack which leads to lower constraint compared to the standard specimen geometry used in determining the cell model parameters. The cell model parameters determined in Chapter 5.2 will be used in all the analyses described below.

5.4.1. Numerical predictions of the effects of residual stresses

In [3] the residual stresses were introduced by pre-loading a notched test specimen see Figure 5.16. The pre-load leads to a stress concentration at the notch with compressive stresses normal to the crack surface. When the specimen is unloaded a residual stress field is introduced due to the plastic deformations during the pre-load. The resulting residual stresses are tensile at the notch since they were compressive during the pre-load. For a more thorough description of the residual stress field and how it is introduced see [3].

Figure 5.16. In-plane compression of notched test specimen.

To correctly model the introduction of the residual stress field a separate FE-model was used. The reason for this was the fact that the FE-model with cell elements would introduce some problem if pre-loaded in compression due to the notch at the crack tip. The crack tip notch would lead to an undesired stress concentration. Therefore a separate FE-model was used in obtaining a correct residual stress field. In the FE-model an element layer was introduced at the crack surface during the pre-load see Figure 5.17, which was removed after unloading of the specimen.

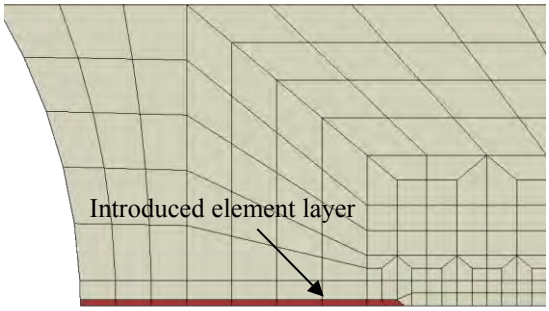

Figure 5.17. Introduced element layer during compressive pre-load.

The stress and strain results from the FE-model without cell elements were then used as pre-scribed initial conditions for the FE-model with cell elements. The resulting residual stress field in the cell element model was compared with the residual stresses in the FE-model without cell elements to verify the procedure of introducing the residual stresses see Figure 5.18. As can be seen in Figure 5.18 the residual stress field agrees well between the two models.

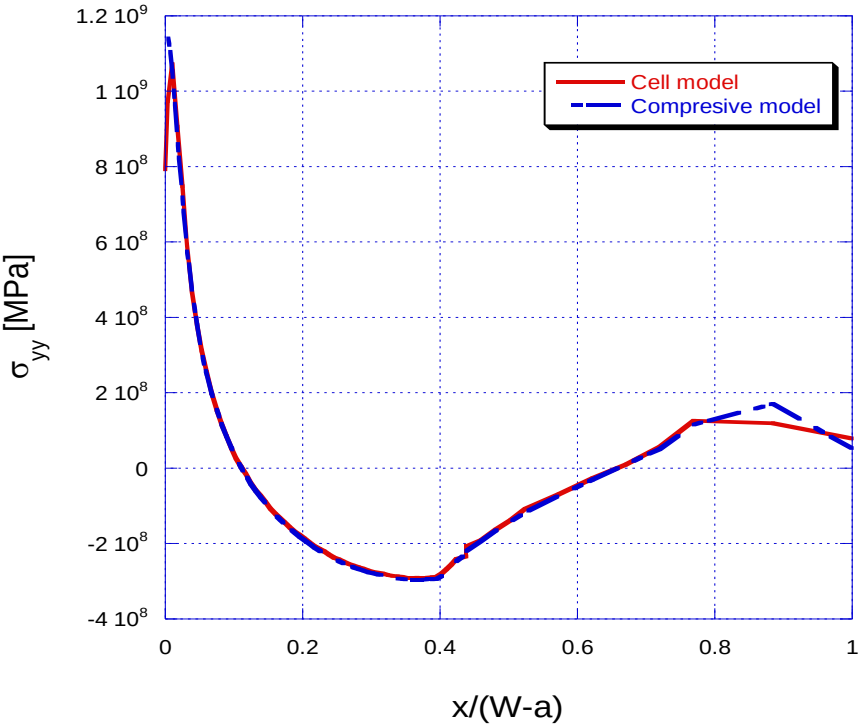

Figure 5.18. Comparison of opening stress along the ligament in front of the crack tip.

Two FE-models were used in the analyses one with and one without residual stresses in order to mimic the experimental setup in [3]. The predicted load-CMOD curves were compared to the experimental results in Figure 5.19. Figure 5.19 shows a very good agreement between the predicted and experimental results leading to a confidence in the correctness of the model and the procedure of introducing the residual stress field.

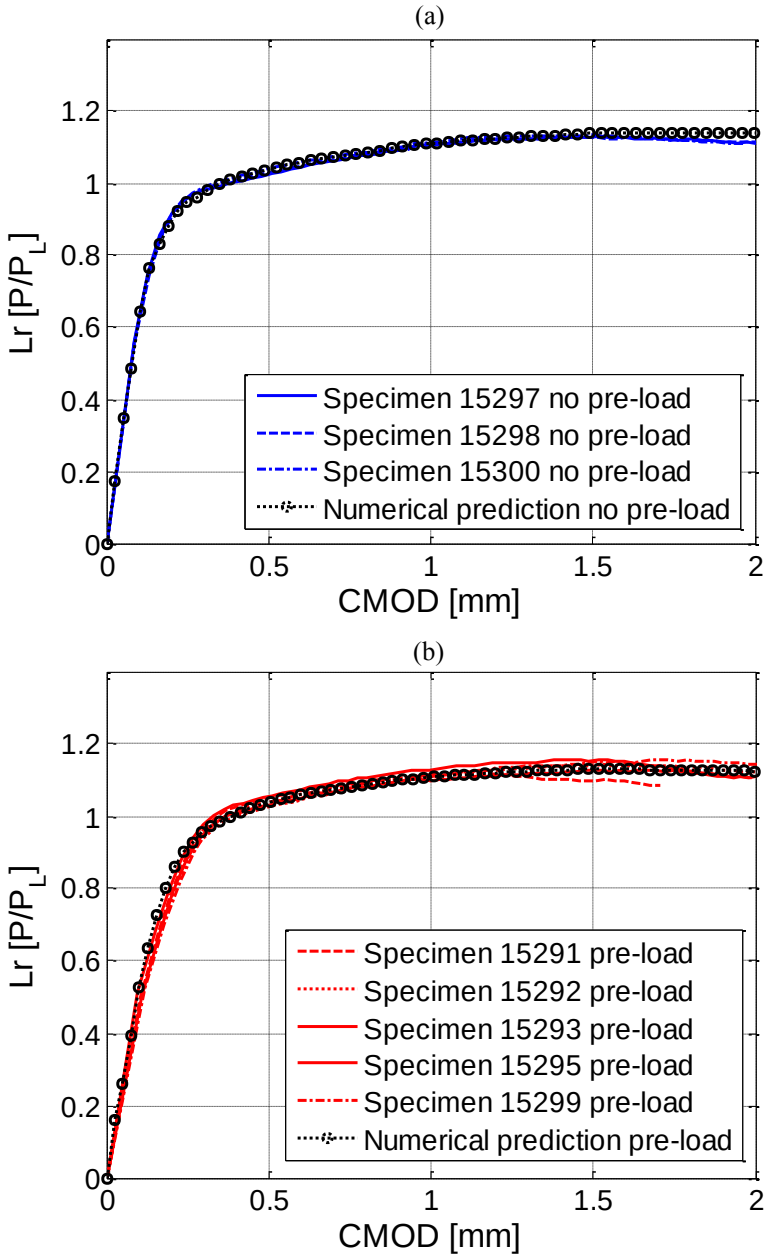

Figure 5.19. Predicted load-CMOD curves compared with the experimental load-CMOD curves for un-grooved notched three point bend specimen, (a) without residual stresses, (b) with residual stresses.

In Figure 5.21 below the predicted J_R-curves from the two FE-models with and without residual stresses are compared to the experimental results from [3]. The experimental results show on a noticeable scatter at larger amount of crack growth. The predicted results lie within the scatter range of the experimental results, though on the upper bound of the scatter. The reason for the upper bound prediction could be due to the low triaxiality at the free surface of the specimens. The Gurson material model underestimates the void growth at low stress triaxiality. Hence the model prediction overestimates the material tearing resistance at the free surface. This effect increases as the crack tunneling becomes more severe as the load increases, hence leading to an overestimated tearing resistance at larger amounts of crack growth. As can be seen in Figure 5.20 the crack tunneling is fairly extensive in

the performed experiments with developed shear lips. The overestimated tearing resistance seen in the predictions can be rectified by using the modified Gurson model which takes in to account the void growth at low triaxiality and for shear dominated states. Further, as for the experimental results, no significant effect from the residual stress field can be seen on crack initiation for the predicted results. Hence it can be concluded that the cell model handles the effect from residual stresses correctly with regards to crack initiation. A small effect on the tearing resistance can be seen at larger amounts of crack growth but it should be noted that this difference falls well within the scatter of the experimental results. These results shows the capability of the cell modeling technique in capturing the effect from residual stresses, though improvements to the predictions can be made with the use of the modified Gurson model. The results in Figure 5.21 also show on the capability of the cell modeling technique in capturing the increased fracture toughness compared to the standard specimen this due to constraint effects.

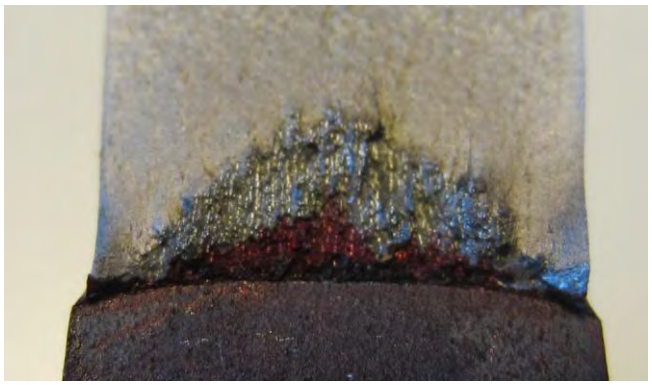

Figure 5.20. Fracture surface of specimen 15295.

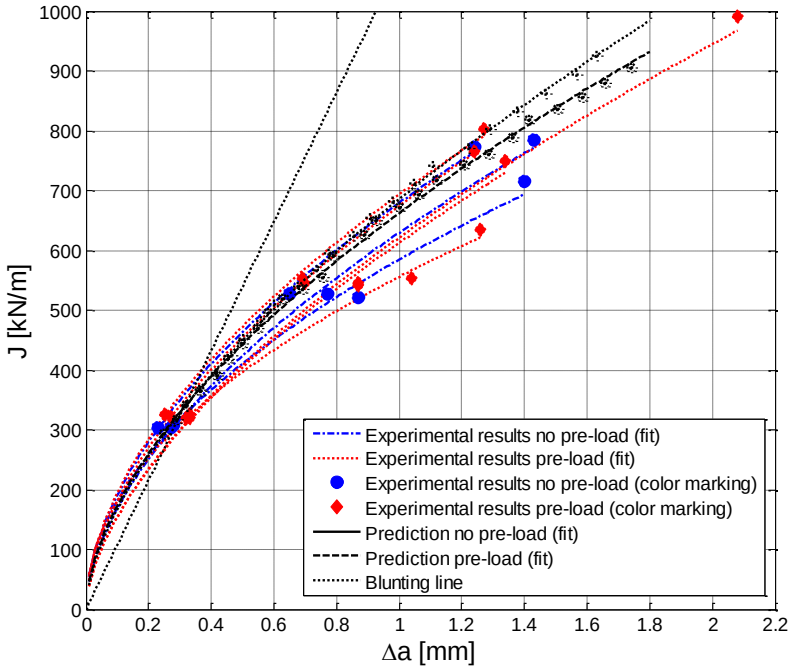

Figure 5.21. Predicted J_R -curves with and without residual stresses compared with the experimental data for un-grooved notched three point bend specimens with and without residual stresses.

In Figure 5.22 the predicted *J*-integral vs. L_r (P/PL) for specimens with and without residual stresses are compared to the experimental results. The predicted results show a very good agreement with the experimental results, recreating the seen effect from the residual stresses on the *J*-integral at low loads and also showing the diminishing effect as the load increases.

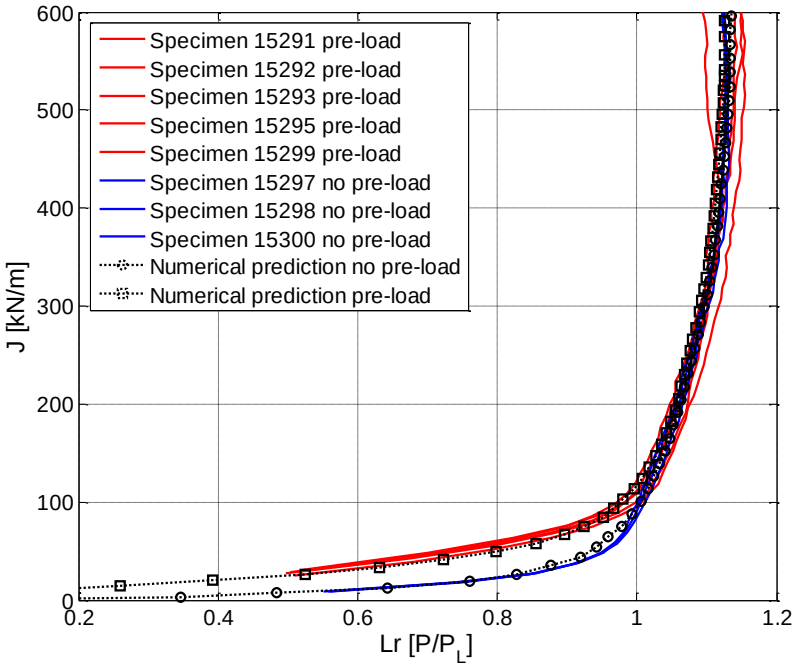

Figure 5.22. Predicted *J* versus L_r results compared to experimentally obtained *J* versus L_r results for un-grooved notched three point bend specimen with and without residual stresses.

6. Discussion of results

From the experimentally evaluated J_R-curves, a large effect on the material fracture toughness is seen for specimens pre-loaded to 6% total strain. This is true for pre-loading in both tension and compression but the effect is larger in the specimens pre-loaded in tension. It can also be concluded that no distinctive effects on J_{Ic} is seen from pre-loading to 1.5 or 3 % total strain. It should be noted that the effects seen, as a result of work hardening, are due to a prior pre-load at room temperature. Hence these effects are not representative for cases were the material exhibits a level of pre-strain caused by welding.

The large effect on the material fracture toughness seen for specimens pre-loaded to 6% total strain is true for pre-loading in both tension and compression, though the effect on the fracture toughness is greater in the specimens pre-loaded in tension. The reason for this could be a result of the forming and growth of micro voids at high tensile pre-loads. This hypothesis is strengthened by the numerical predictions shown in Chapter 5.3 where a clear effect of a possible void volume growth due to high pre-load level is seen, see Figure 5.14. This possible effect is very limited at lower pre-load levels this is also true for the experimental results.

The computational work done in Chapter 5 have shown that numerical predictions of cracked geometries, other than the specimen geometry used in determining the material parameters, give good results, with some exceptions that are attributable to other factors, using the same determined material parameters. Hence the scheme outlined by Faleskog et al. [1] and Gao et al. [2] to determine the material parameters based on a uniaxial tensile test and a standard fracture test is shown to be a structured and sound approach.

Further the numerically obtained crack front profile and the experimental crack front profile correlate with the exception of regions near the free surface. This is explained by the fact that the Gurson material model underestimates the void growth at low stress triaxiality. This can be rectified by using a modified Gurson model which takes in to account the void growth at low triaxiality and for shear dominated states. This is also planned to be done in a future extension of this project. Further improvements to the predictions done by the cell model in Chapter 5.3 could be done by developing a user subroutine describing the Gurson material model with kinematic hardening. This would potentially lead to a possibility to predict the seen effects at high pre-load levels which the current Gurson-model, using isotropic hardening, does not. The problem with using an isotropic hardening material model is evident if the predicted load-CMOD curves are compared with the experimental see Figure 5.12 and Figure 5.15. Nevertheless the cell model gives good predictions of the experimentally generated J_R-curves for pre-load levels up to 3% in both compression and tension.

The cell model does also capture the effects attributable to residual stresses, seen in the experimental work by Bolinder et al. [3]. From the predicted results presented in Chapter 5.4 the same conclusions that were made from the experimental results in [3] can be drawn in regards to fracture toughness and the decreasing influence on the J-integral for increasing primary load, although the predictions made here could be further improved. The predicted J_R-curves for the nonstandard specimens with and without residual stresses lie within the scatter range of the experimental results, though on the upper bound of the scatter. The reason for the upper bound prediction of the J_R-curves for nonstandard specimens with and without residual stresses is due to the low triaxiality at the free surface of the specimens. The Gurson material model underestimates the void growth at low stress triaxiality hence leading to an overestimated tearing resistance at the free surfaces. This can be rectified, as discussed above, by using a modified Gurson model which takes in to account the void growth at low triaxiality and for shear dominated states.

The report has shown on the capability of the cell model in capturing the effects on ductile tearing from limited pre-load levels and a residual stress field. Nevertheless there have also been seen possibilities of improvements by using a modified Gurson model which takes into account the void growth at low triaxiality and shear dominated states and the need for a cell model using a kinematic material hardening.

7. Conclusion

From the numerical and experimental results presented in this report it can be concluded that:

- For specimens pre-loaded (work hardened) to 6% of total strain at room temperature in both tension and compression large effects are seen on both the tearing resistance and crack initiation. Note though that the effect on the fracture toughness is greater in the specimens pre-loaded in tension.
- No distinctive influence on the material fracture toughness is observed from pre-loading (work hardening), both tensile and compressive, at room temperature of 1.5 or 3 % total strain.
- The cell model gives good predictions of the experimentally generated JR-curves for pre-load levels up to 3% in compression and tension. As for the experimental results, no significant effect from the pre-load (work hardening) on the fracture resistance is seen for pre-load levels up to 3%.
- The predicted results overestimate the material fracture toughness for pre-load levels of 6%. The seen effect from the experimental results at a pre-load level of 6% is much larger than the predicted effect both for compression and tension. Hence the current cell model fails to accurately capture the large effects seen at higher levels of pre-load.
- At a pre-load level of 1.5% the effect on the crack growth resistance, due to void volume growth, is insignificant but as the pre-load level increases up to 6% the seen effect is substantially increased. This is a trend that also can be seen in the difference between the experimental results pre-loaded in compression and tension.
- The cell model do capture the effects attributable to residual stresses, seen in the experimental work by Bolinder et al. [3], in regards to fracture toughness and the decreasing influence on the J-integral for increasing primary load.
- The results in Figure 5.21 also shows the capability of the Gurson model to capture the increased fracture toughness compared to the standard specimen which is due to constraint effects.

8. Future work

A continuation of the presented work is planned. In this continuation the possibilities of improvements that have been made evident in the presented work will be explored. A modified Gurson model which takes into account the void growth at low triaxiality and shear dominated states will be used to potentially give more accurate predictions of the J_R-curves and the shape of the crack front. Furthermore complementary experiments will be conducted, this to give a deeper understanding of the behavior for the used material A533B. There is also the ambition to complement the modified Gurson model with the option to use kinematic material hardening. To be able to use kinematic hardening could possibly make it possible to correctly predict the seen effect on the J_R-curves from high pre-load levels.

Further in the future it is the ambition to use the modified Gurson model in studying the effect of residual stresses on ductile tearing at low primary loads, specifically to study the effect on the residual stresses from a limited and stable crack growth.

The modified Gurson model could also be used in designing experiments, this to avoid undesired and unpredictable test results and to be certain that the experiments give relevant results.

For irradiated materials it is often very hard to obtain material with large enough dimensions, which can meet the size requirements, imposed by testing standards. Therefore this could be one possible application for the modified Gurson model. The modified Gurson model could be used to examine the size effects when using small fracture test specimens. This to be able to correctly interpret the results obtained from small fracture test specimens of irradiated material.

9. References

[1] J. Faleskog, X. Gao, and C.F. Shih, "Cell model for nonlinear fracture analysis – I. Micromechanics calibration," *International Journal of Fracture*, vol. 89, pp. 355-373, 1998.

[2] X. Gao, J. Faleskog, and C.F. Shih, "Cell model for nonlinear fracture analysis – II. Fracture-process calibration and verification," *International Journal of Fracture*, vol. 89, pp. 375-398, 1998.

[3] T. Bolinder and I. Sattari-Far, "Experimental evaluation of influence from residual stresses on crack initiation and ductile crack growth at high primary loads," Swedish Radiation Safety Authority, Report number 2009:27, 2011.

[4] P. Dillström, M. Andersson, I. Sattari-Far, and W. Zhang, "Analysis strategy for fracture assessment of defects in ductile material," Swedish Radiation Safety Authority, Report number 2009:27, 2009.

[5] X. Gao, J. Faleskog, and C.F. Shih, "Ductile tearing in part-through cracks: experiments and cell model predictions," *Engineering Fracture Mechanics*, vol. 59, no. 6, pp. 761-777.

[6] L. Xia and C.F. Shih, "Ductile crack growth - I. A numerical study using coputational cells with a microstructurally-based length scale," *Journal of the Mechanics and Physics of Solids*, vol. 43, pp. 233-259, 1995.

[7] L. Xia and C.F. Shih, "Ductile crack growth - II. Void nucleation and geometry effects on microscopic fracture behavior," *Journal of the Mechanics and Physics of Solids*, vol. 43, pp. 1953-1981, 1995.

[8] A.L. Gurson, "Continuum theory of ductile rupture by void nucleation an growth: Part I – Yield criteria and flow rules for porous ductile media," *Journal of Engineering Materials and Technology*, vol. 99, pp. 2-15, 1977.

[9] V. Tvergaard, "Material failure by void growth to coalescence," *Advances in applied Mechanics*, no. 27, pp. 83-151, 1990.

[10] Hibbit, Karlsson, and Sorenson, *ABAQUS user manual*.: Dassault Systèmes.

[11] V. Tvergaard and A. Needleman, "Analysis of cup-cone fracture in a round tensile bar.," *Acta Metallurgica*, vol. 32, pp. 157-169, 1984.

[12] C.F. Shih, "Relationship between the J-integral and the crack opening displacement for stationary and extending cracks," *Journal of the Mechanics and Physics of Solids*, vol. 29, pp. 305-326, 1981.

[13] "Standard test method of measurement of fracture toughness," ASTM, E 1820,.

[14] S. Sivaprasad, S. Tarafder, V.R. Ranganath, and K.K. Ray, "Effect of prestrain on fracture toughness of HSLA steels," *Material Science and Engineering*, vol. A284, pp. 195-201, 2000.

[15] P.K. Liaw and J.D. Landes, "Influence of prestrain history on fracture toughness properties of steels," *Metallurgical Transactions A*, vol. 17, pp. 473-489, 1986.

[16] X. Qian, "An out-of-plane length scale for ductile crack extensions in 3-D SSY model for X65 pipeline materials," *International Journal of Fracture*, vol. 167, pp. 249-265, 2011.

Appendix A

In appendix A the P-CMOD curves for each specimen are presented. The specimen numbers and pre-load are listed below.

Specimen list:

15825	no pre-load	Figure A.1
15826	no pre-load	Figure A.2
15827	1.5 % compressive pre-load	Figure A.3
15828	1.5 % compressive pre-load	Figure A.4
15829	3.0 % compressive pre-load	Figure A.5
15830	3.0 % compressive pre-load	Figure A.6
15831	6.0 % compressive pre-load	Figure A.7
15832	6.0 % compressive pre-load	Figure A.8
15833	1.5 % tensile pre-load	Figure A.9
15834	1.5 % tensile pre-load	Figure A.10
15835	3.0 % tensile pre-load	Figure A.11
15836	3.0 % tensile pre-load	Figure A.12
15837	6.0 % tensile pre-load	Figure A.13
15838	6.0 % tensile pre-load	Figure A.14

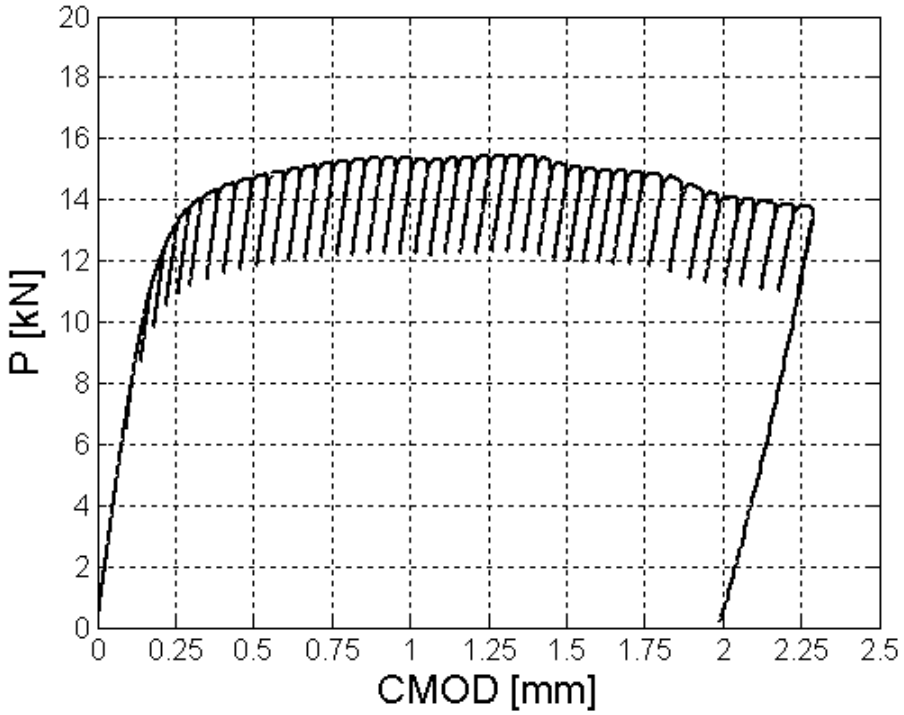

Figure A.1. P-CMOD curve for specimen 15825 no pre-load.

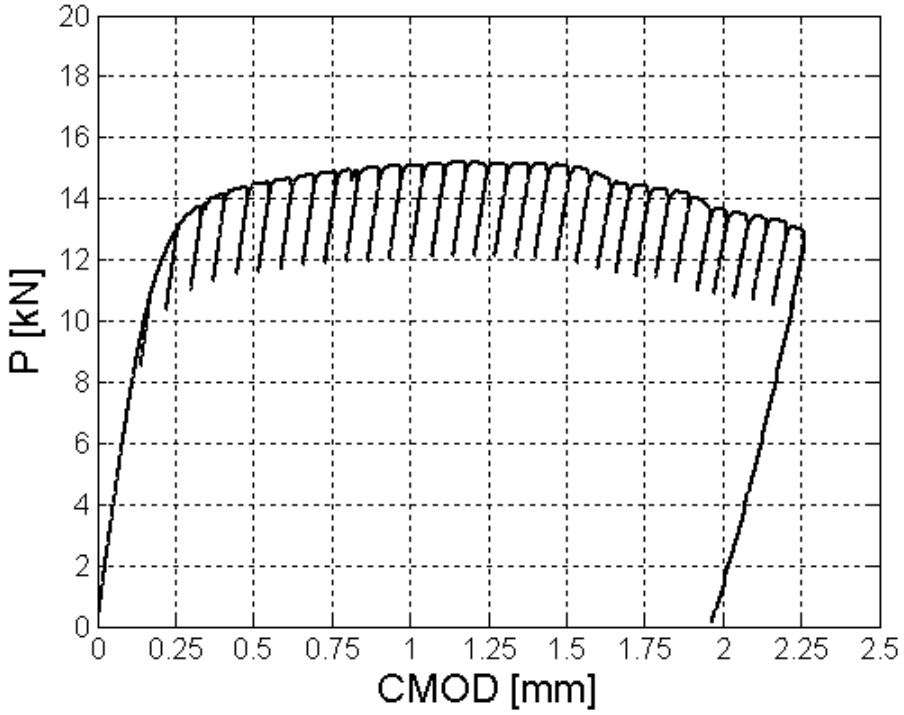

Figure A.2. P_CMOD curve for specimen 15826 no pre-load.

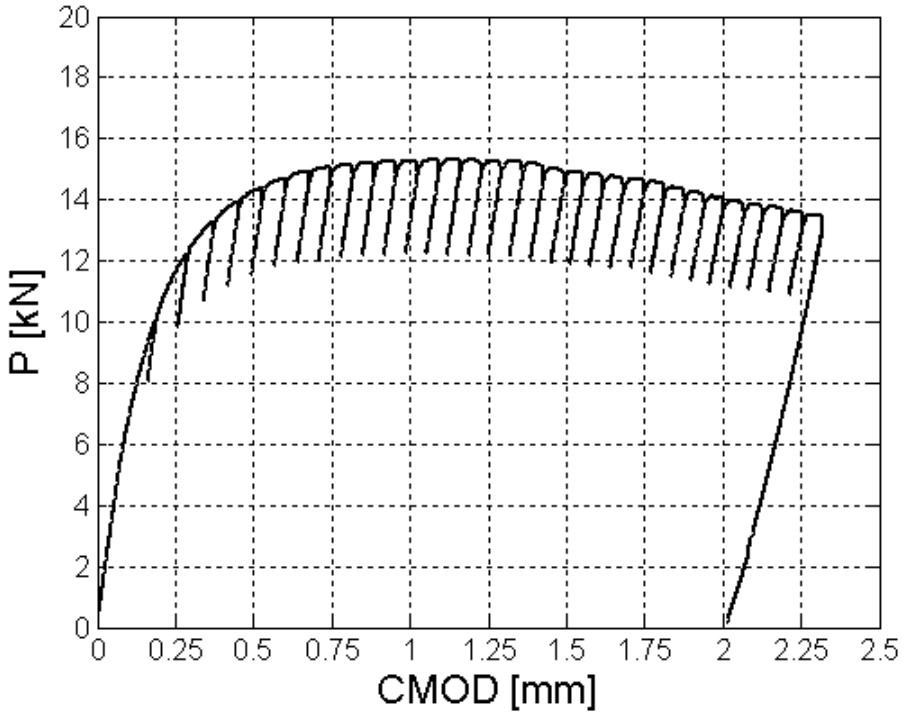

Figure A.3. P_CMOD curve for specimen 15827 1.5 % compressive pre-load.

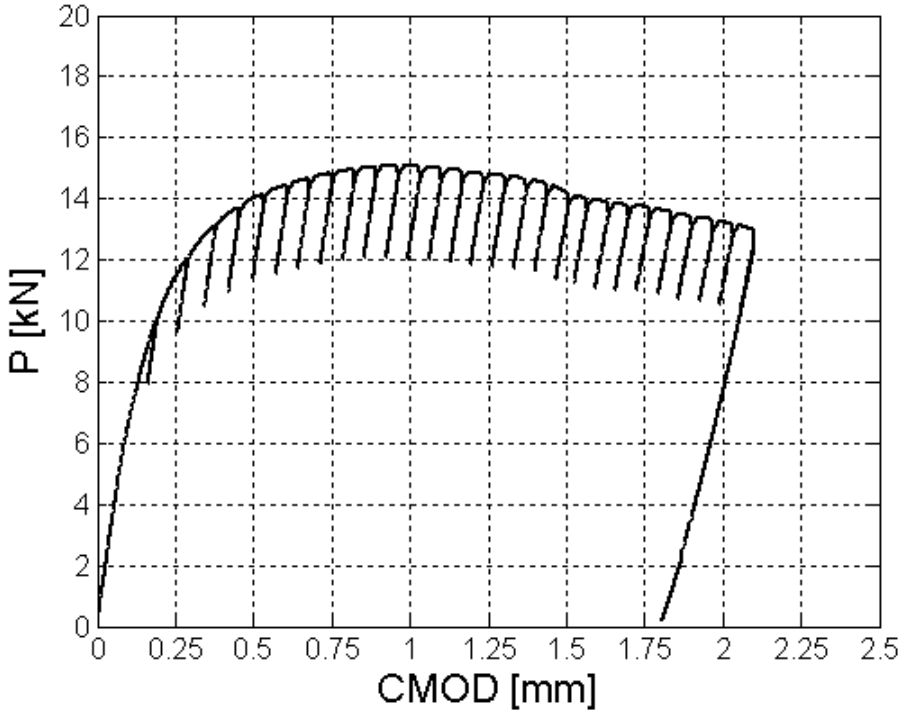

Figure A.4. P_CMOD curve for specimen 15828 1.5 % compressive pre-load.

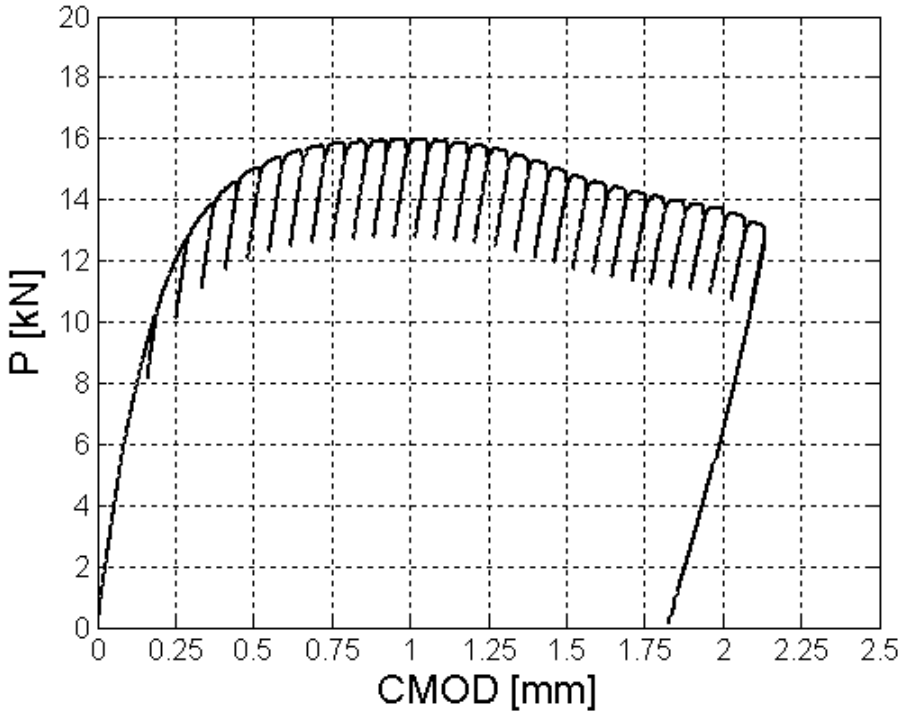

Figure A.5. P_CMOD curve for specimen 15829 3.0 % compressive pre-load.

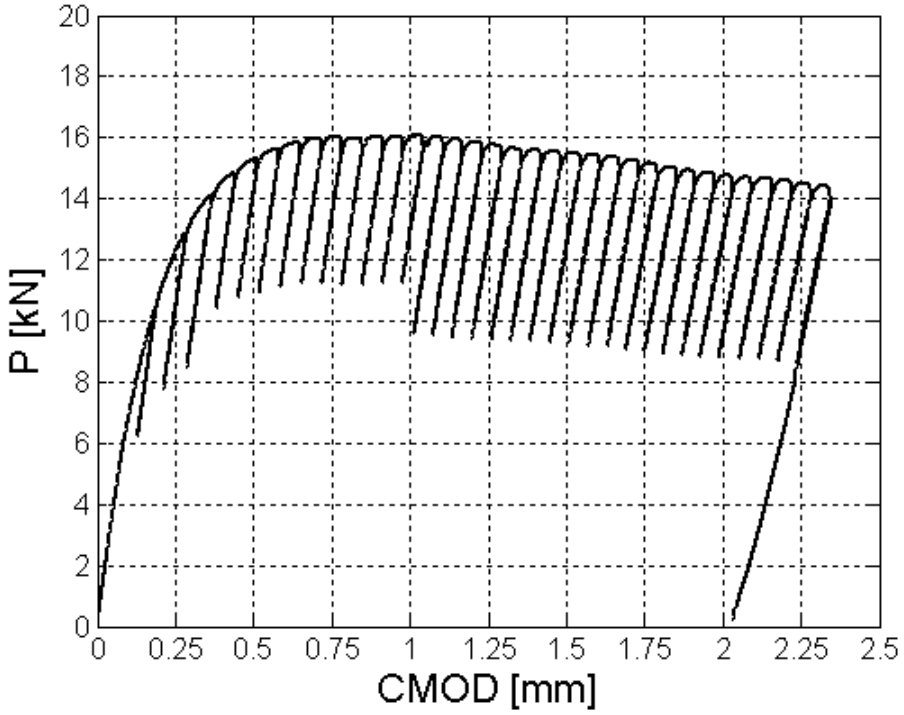

Figure A.6. P_CMOD curve for specimen 15830 3.0 % compressive pre-load.

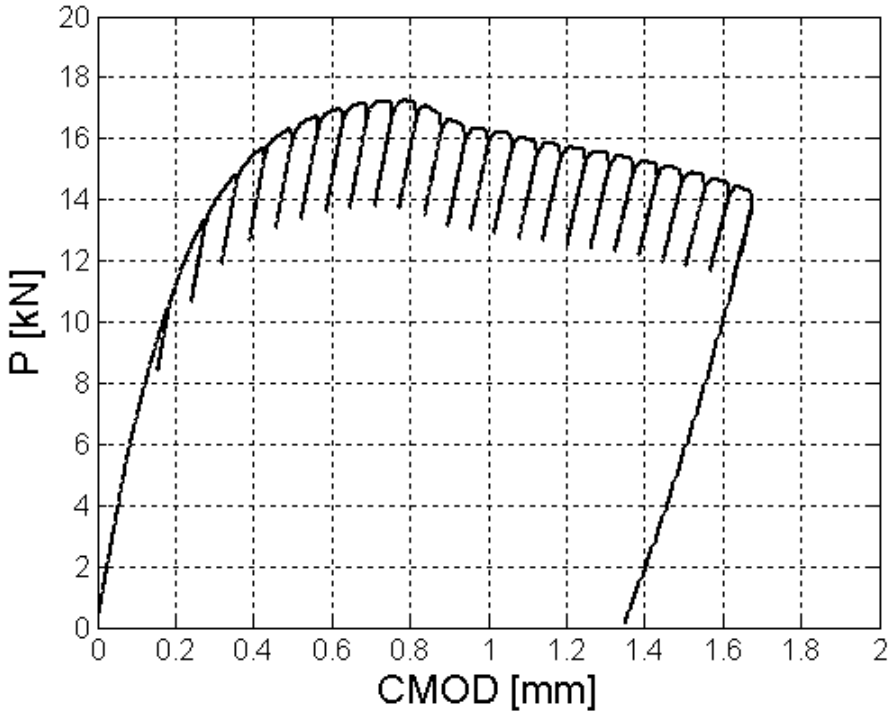

Figure A.7. P_CMOD curve for specimen 15831 6.0 % compressive pre-load.

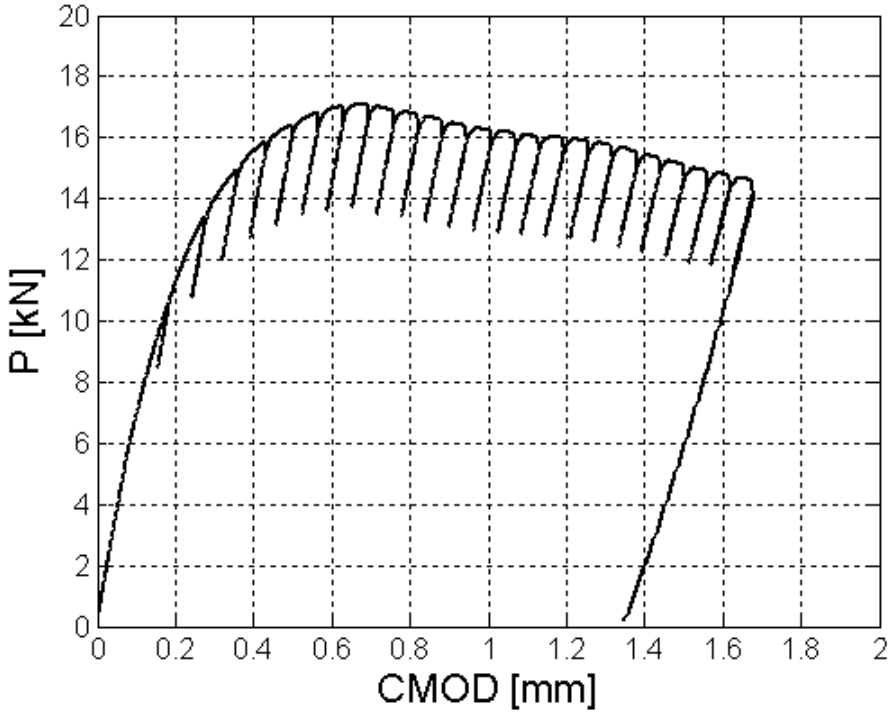

Figure A.8. P_CMOD curve for specimen 15832 6.0 % compressive pre-load.

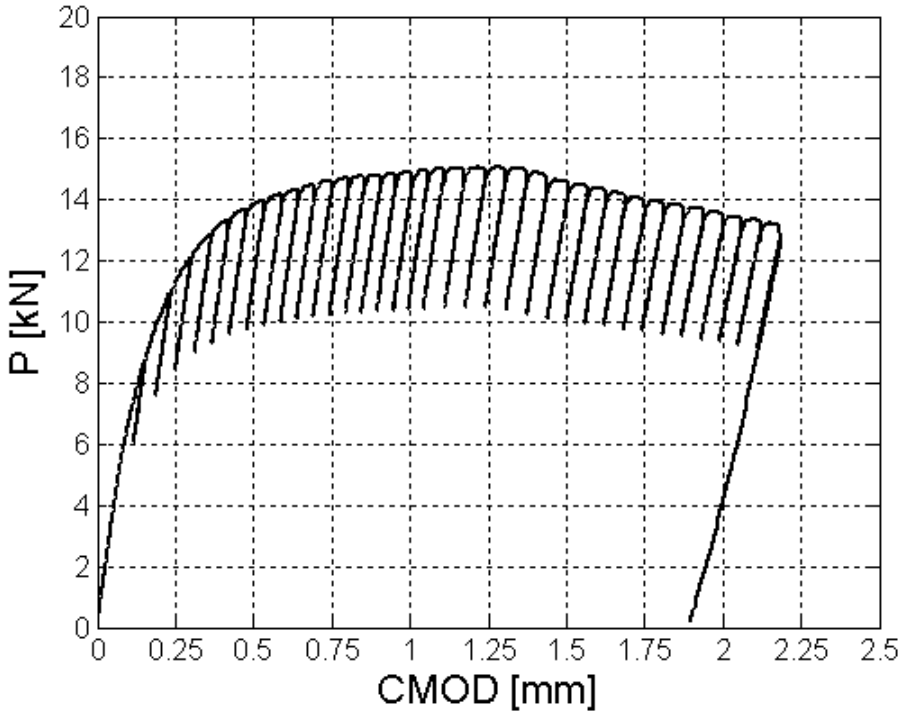

Figure A.9. P_CMOD curve for specimen 15833 1.5 % tensile pre-load.

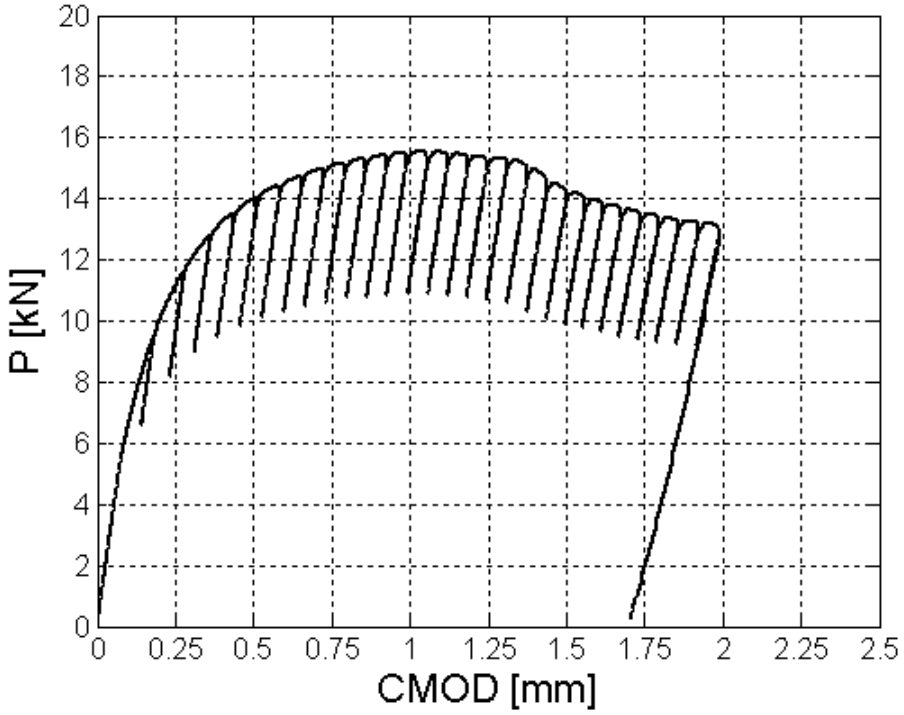

Figure A.10. P_CMOD curve for specimen 15834 1.5 % tensile pre-load.

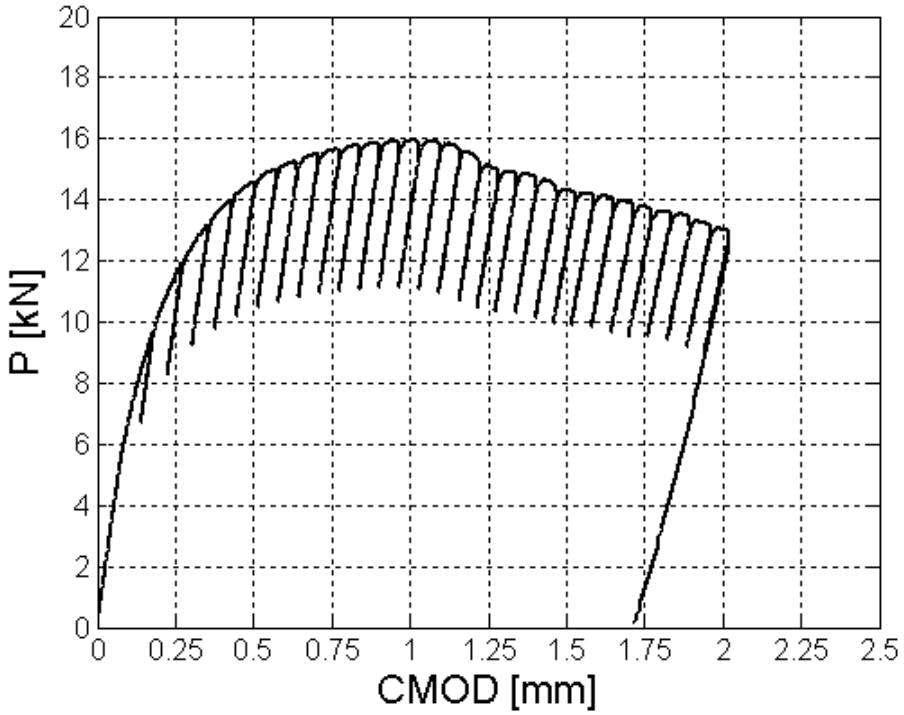

Figure A.11. P_CMOD curve for specimen 15835 3.0 % tensile pre-load.

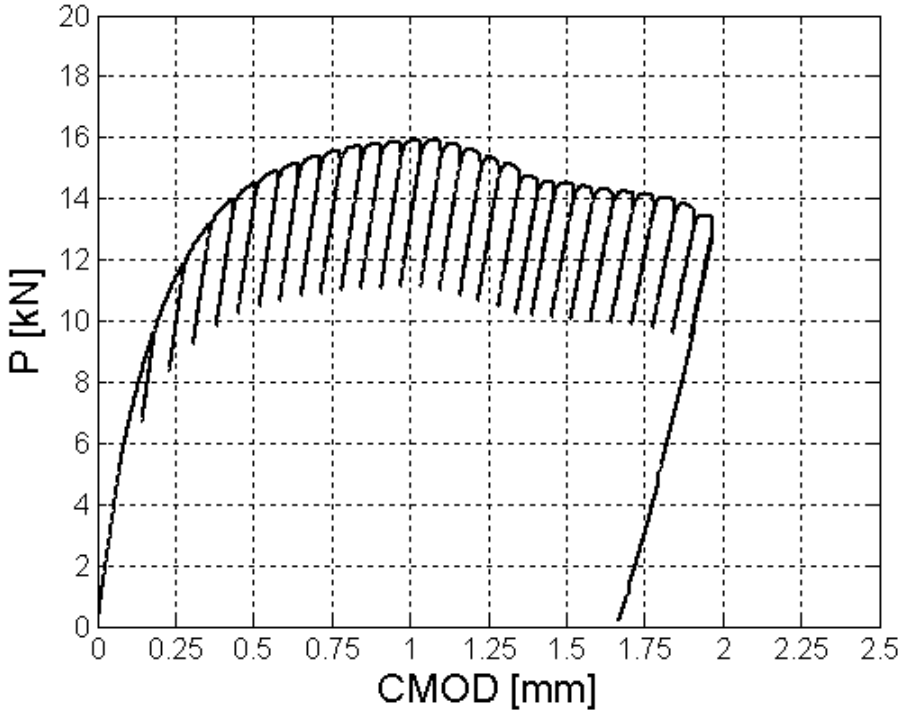

Figure A.12. P_CMOD curve for specimen 15836 3.0 % tensile pre-load.

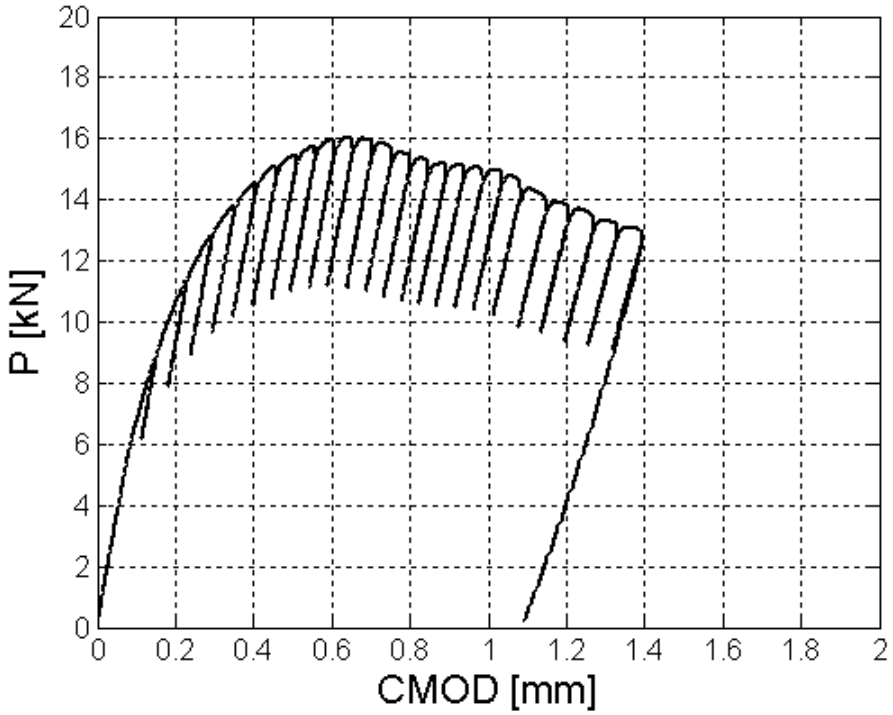

Figure A.13. P_CMOD curve for specimen 15837 6.0 % tensile pre-load

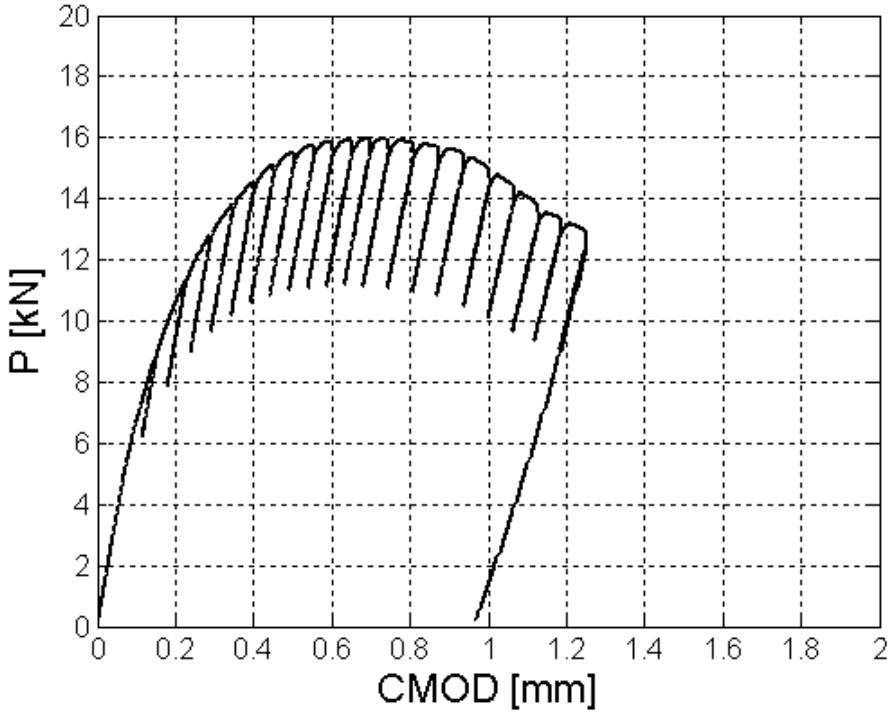

Figure A.14. P_CMOD curve for specimen 15838 6.0 % tensile pre-load

Appendix B

In Appendix B the *J-R* evaluations for each specimen are presented. The specimen numbers and pre-load are listed below.

Specimen list:

FRACTURE TOUGHNESS TEST - J_{Ic} according to ASTM E 1820

Specimen no.	15825J			
Label				
Task	Bolinder			
Type	SENB	W=26.98 mm	B=13.52 mm	B_n=10.78 mm
Material	Obelastad			
Temperature	rt °C			
Yield stress	500 MPa			
Precracking max	3.7 kN			
Loading rate	1.71 (Limit load)/(minute)			
Fatigue crack	13.54 mm			
Max. crack deviation	0.40			
Crack extension	2.10 mm			
Estimated a0q	13.41 mm			

J_{Ic} = 249 kN/m

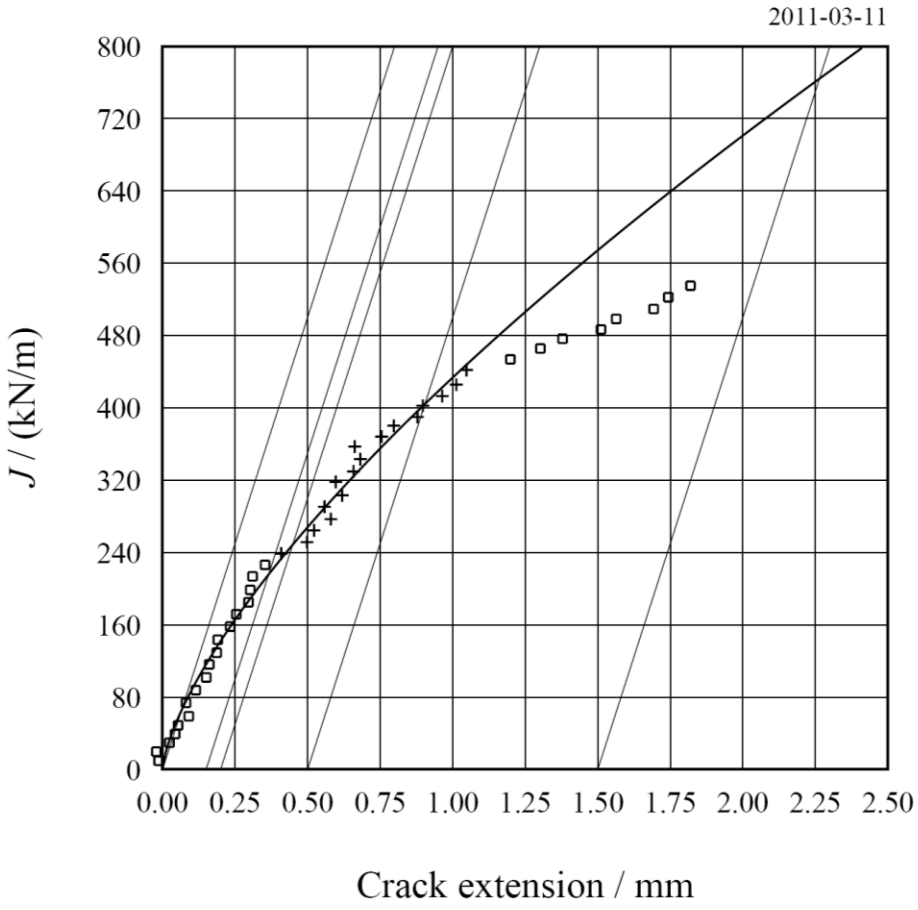

FRACTURE TOUGHNESS TEST - J_{Ic} according to ASTM E 1820

Specimen no.	15826j			
Label				
Task	Bolinder			
Type	SENB	W=26.97 mm	B=13.53 mm	B_n=10.96 mm
Material	Obelastad			
Temperature	rt °C			
Yield stress	540 MPa			
Precracking max	3.7 kN			
Loading rate	1.74 (Limit load)/(minute)			
Fatigue crack	13.67 mm			
Max. crack deviation	0.16			
Crack extension	2.20 mm			
Estimated a0q	13.60 mm			

J_{Ic} = 262 kN/m

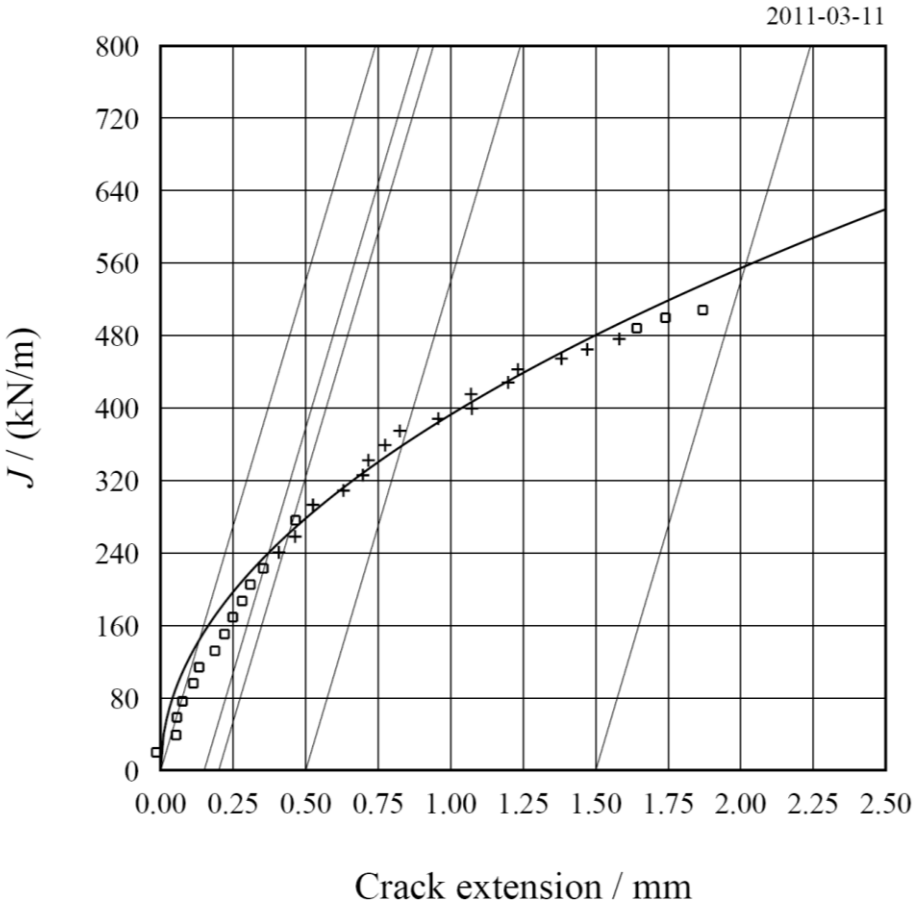

FRACTURE TOUGHNESS TEST - J_{Ic} according to ASTM E 1820

Specimen no.	15827J			
Label	T1.5			
Task	Bolinder			
Type	SENB	W=26.96 mm	B=13.53 mm	B_n=10.77 mm
Material	tryck 1,5 %			
Temperature	rt °C			
Yield stress	540 MPa			
Precracking max	3.7 kN			
Loading rate	1.84 (Limit load)/(minute)			
Fatigue crack	13.84 mm			
Max. crack deviation	0.52			
Crack extension	1.94 mm			
Estimated a0q	13.68 mm			

J_{Ic} = 249 kN/m

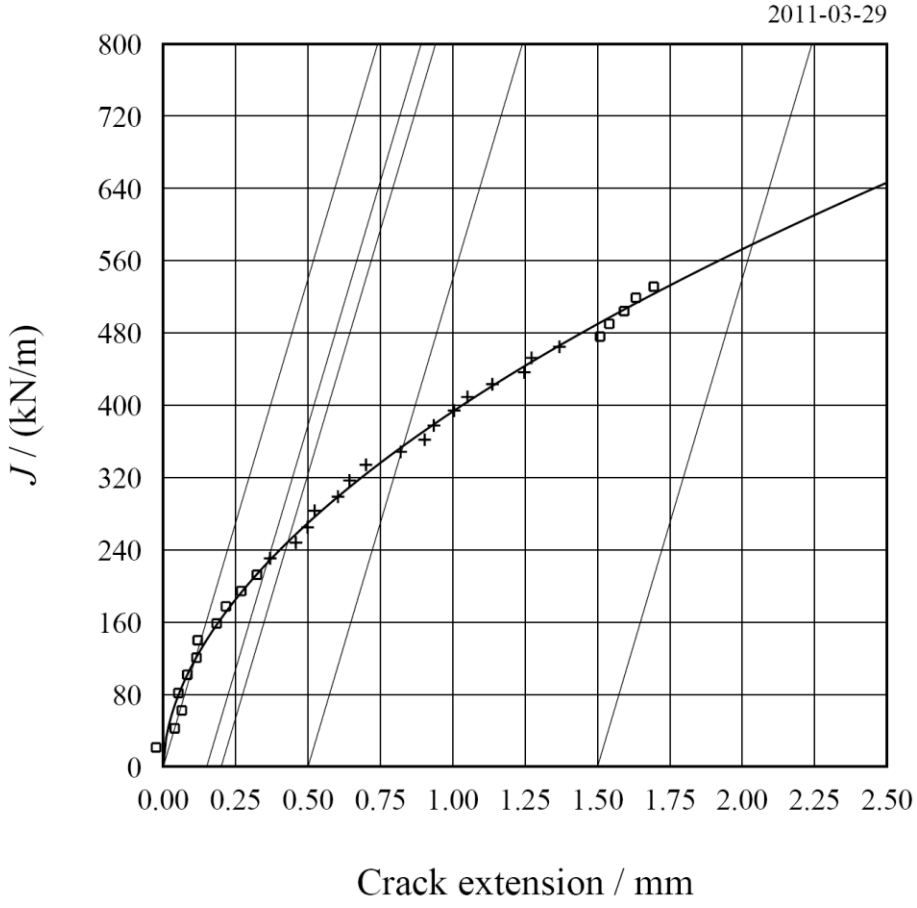

FRACTURE TOUGHNESS TEST - J_{Ic} according to ASTM E 1820

Specimen no.	15828j			
Label	T1.5			
Task	Bolinder			
Type	SENB	W=26.96 mm	B=13.48 mm	B_n=10.67 mm
Material	Tryck 1,5 %			
Temperature	rt °C			
Yield stress	540 MPa			
Precracking max	3.7 kN			
Loading rate	1.83 (Limit load)/(minute)			
Fatigue crack	13.87 mm			
Max. crack deviation	0.67			
Crack extension	1.88 mm			
Estimated a0q	13.71 mm			

J_{Ic} = 235 kN/m

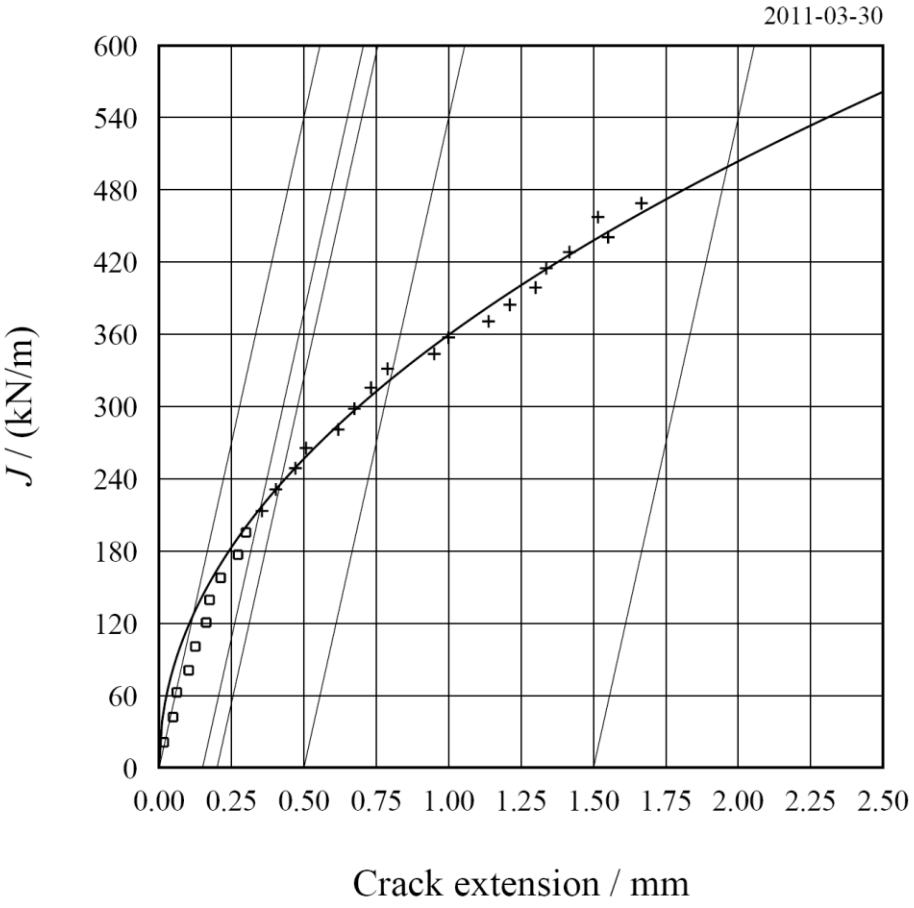

FRACTURE TOUGHNESS TEST - J_{Ic} according to ASTM E 1820

Specimen no.	15829J			
Label	T3			
Task	Bolinder			
Type	SENB	W=26.99 mm	B=13.48 mm	B_n=10.86 mm
Material	Tryck 3 %			
Temperature	rt °C			
Yield stress	540 MPa			
Precracking max	3.7 kN			
Loading rate	1.79 (Limit load)/(minute)			
Fatigue crack	13.86 mm			
Max. crack deviation	0.40			
Crack extension	2.00 mm			
Estimated a0q	13.78 mm			

J_{Ic} = 256 kN/m

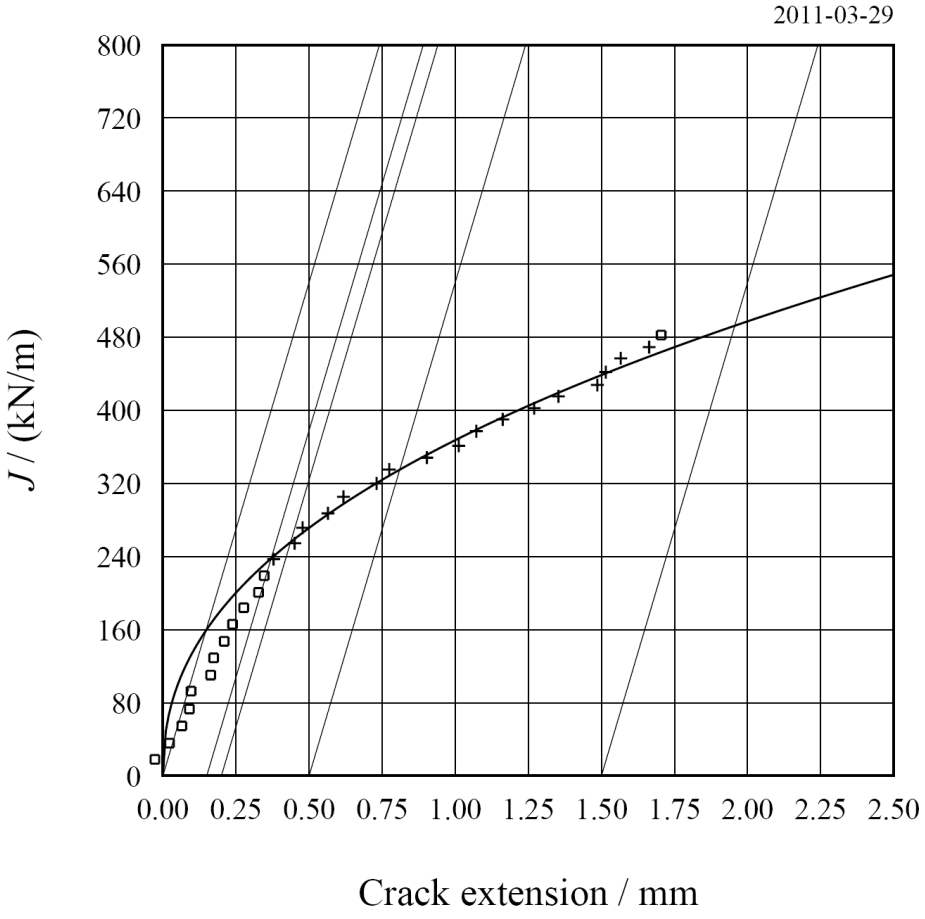

FRACTURE TOUGHNESS TEST - J_{Ic} according to ASTM E 1820

Specimen no.	15830j			
Label	T3			
Task	Bolinder			
Type	SENB	W=27.00 mm	B=13.47 mm	B_n=10.93 mm
Material	Tryck 3 %			
Temperature	rt °C			
Yield stress	540 MPa			
Precracking max	3.7 kN			
Loading rate	1.81 (Limit load)/(minute)			
Fatigue crack	13.83 mm			
Max. crack deviation	0.44			
Crack extension	1.63 mm			
Estimated a0q	13.76 mm			

J_{Ic} = 220 kN/m

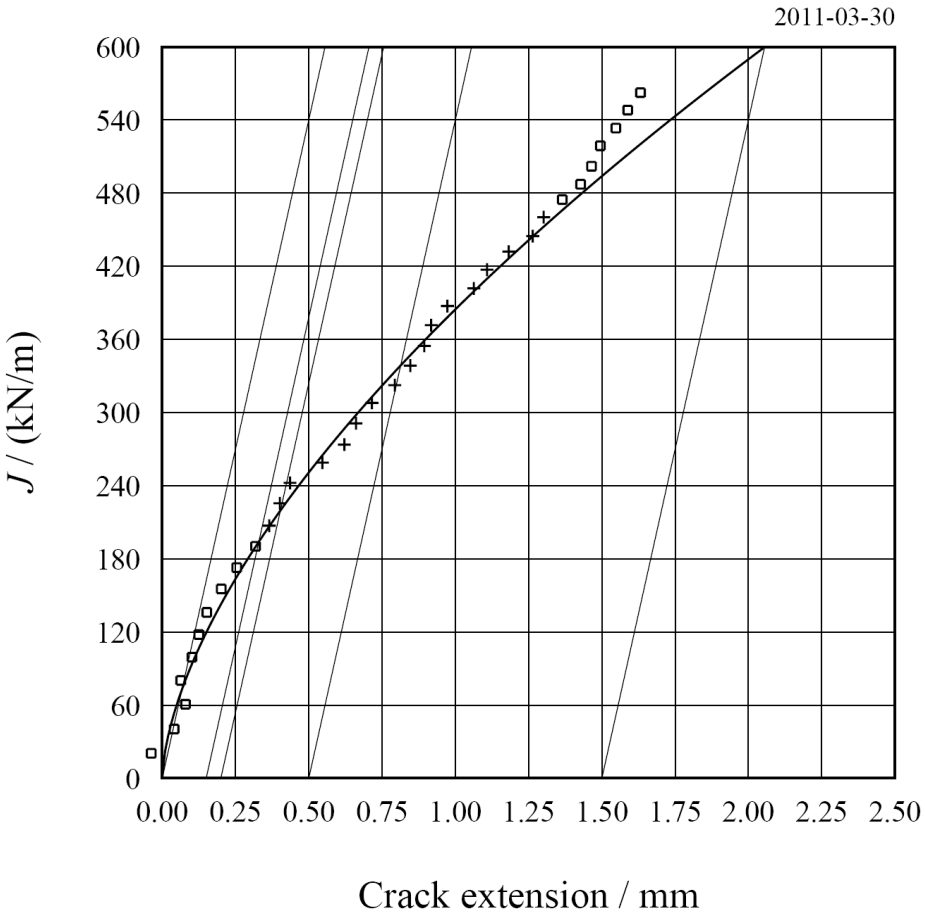

FRACTURE TOUGHNESS TEST - J_{Ic} according to ASTM E 1820

Specimen no.	15831J			
Label	T6			
Task	Bolinder			
Type	SENB	W=27.00 mm	B=13.43 mm	B_n=10.66 mm
Material	Tryck 6 %			
Temperature	rt °C			
Yield stress	540 MPa			
Precracking max	3.7 kN			
Loading rate	1.77 (Limit load)/(minute)			
Fatigue crack	13.72 mm			
Max. crack deviation	0.45			
Crack extension	1.63 mm			
Estimated a0q	13.63 mm			

J_{Ic} = 170 kN/m

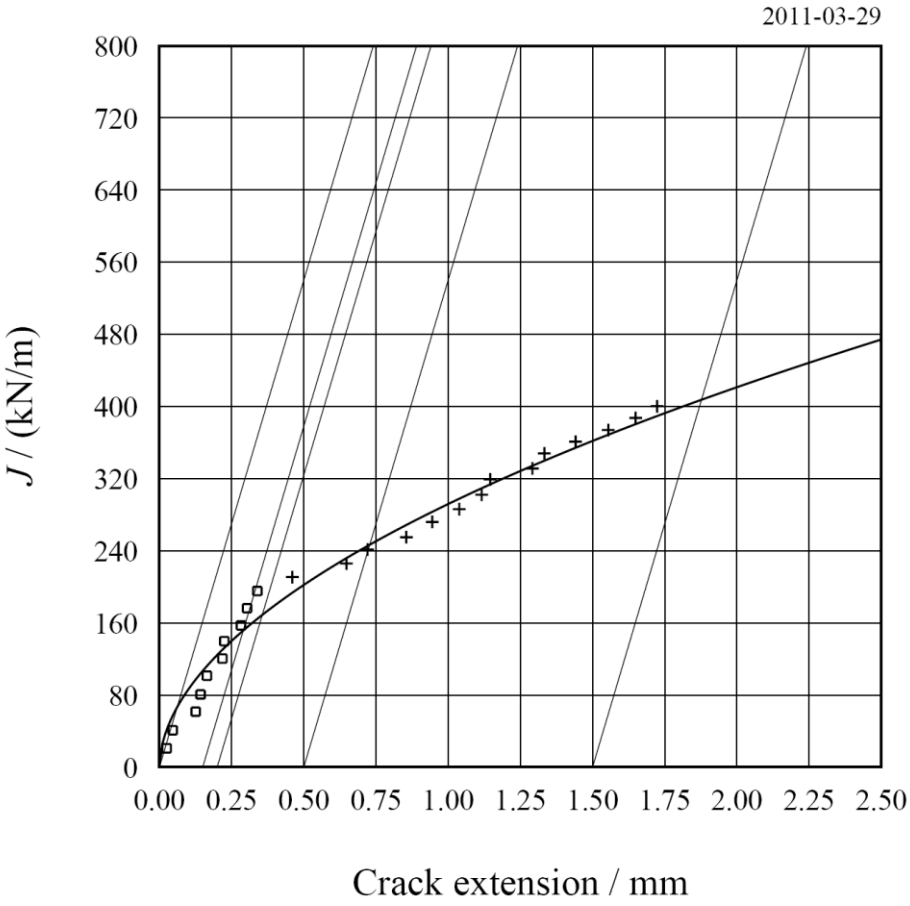

FRACTURE TOUGHNESS TEST - J_{Ic} according to ASTM E 1820

Specimen no.	15832j			
Label	T6			
Task	Bolinder			
Type	SENB	W=26.97 mm	B=13.49 mm	B_n=10.76 mm
Material	Tryck 6 %			
Temperature	rt °C			
Yield stress	540 MPa			
Precracking max	3.7 kN			
Loading rate	1.74 (Limit load)/(minute)			
Fatigue crack	13.64 mm			
Max. crack deviation	0.43			
Crack extension	1.68 mm			
Estimated a0q	13.56 mm			

J_{crit} = 163 kN/m

- estimation of a0q not valid
- final crack front too curved

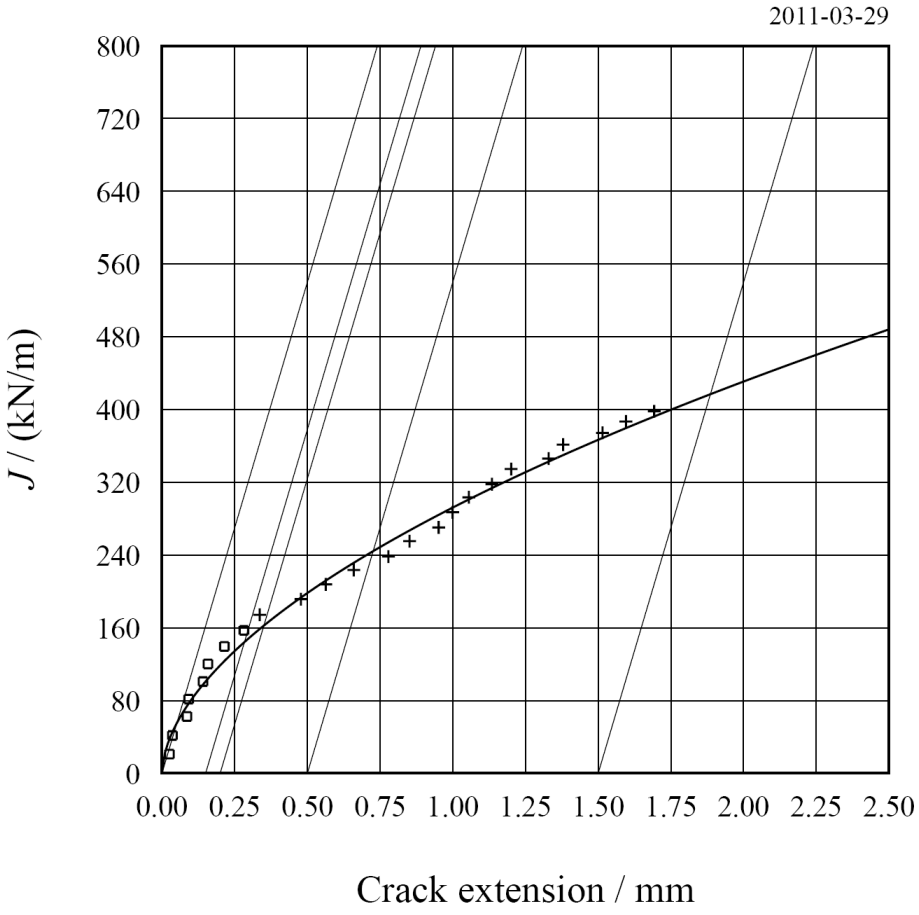

FRACTURE TOUGHNESS TEST - J_{Ic} according to ASTM E 1820

Specimen no.	15833J			
Label	D1.5			
Task	Bolinder			
Type	SENB	W=26.96 mm	B=13.45 mm	B_n=10.78 mm
Material	A533B-1			
Temperature	rt °C			
Yield stress	540 MPa			
Precracking max	14 kN			
Loading rate	1.77 (Limit load)/(minute)			
Fatigue crack	13.76 mm			
Max. crack deviation	0.49			
Crack extension	2.11 mm			
Estimated a0q	13.69 mm			

J_{crit} = 270 kN/m

- final crack front too curved
- crack extension measurement error = 0.059 mm too high

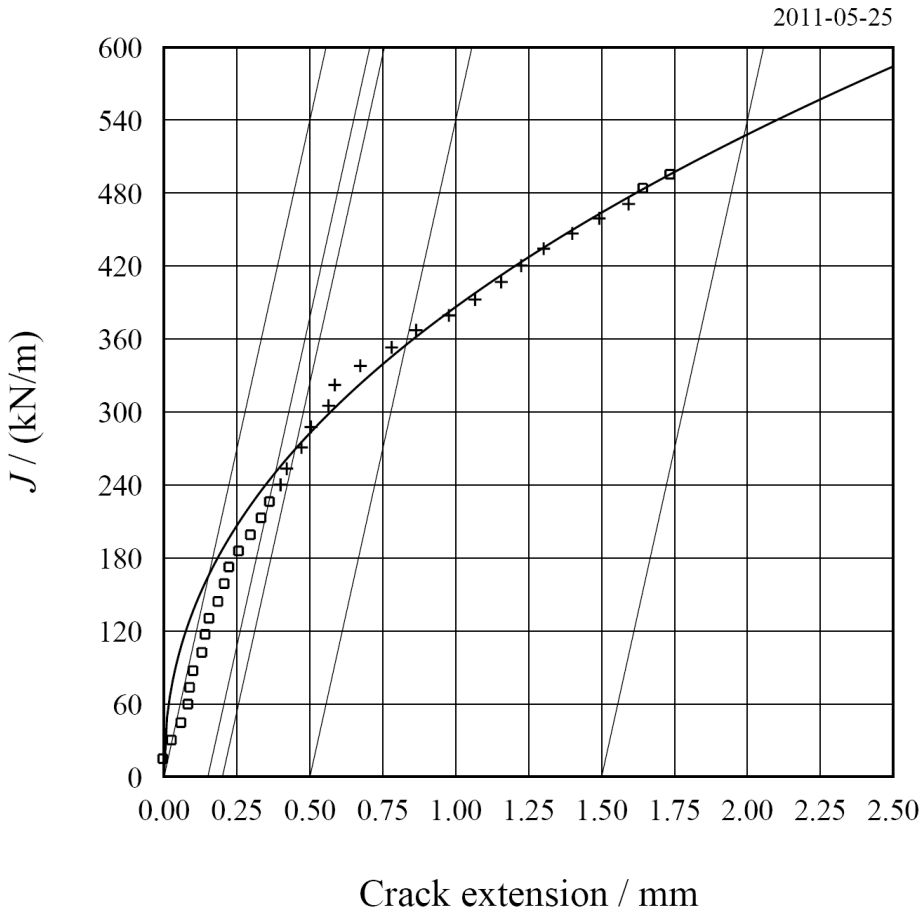

FRACTURE TOUGHNESS TEST - J_{Ic} according to ASTM E 1820

Specimen no.	15834j			
Label	D1.5			
Task	Bolinder			
Type	SENB	W=26.95 mm	B=13.45 mm	B_n=10.79 mm
Material	A533B-1			
Temperature	rt °C			
Yield stress	540 MPa			
Precracking max	14 kN			
Loading rate	1.67 (Limit load)/(minute)			
Fatigue crack	13.58 mm			
Max. crack deviation	0.32			
Crack extension	2.30 mm			
Estimated a0q	13.50 mm			

J_{crit} = 279 kN/m

- estimation of a0q not valid
- crack extension measurement error = 0.262 mm too high

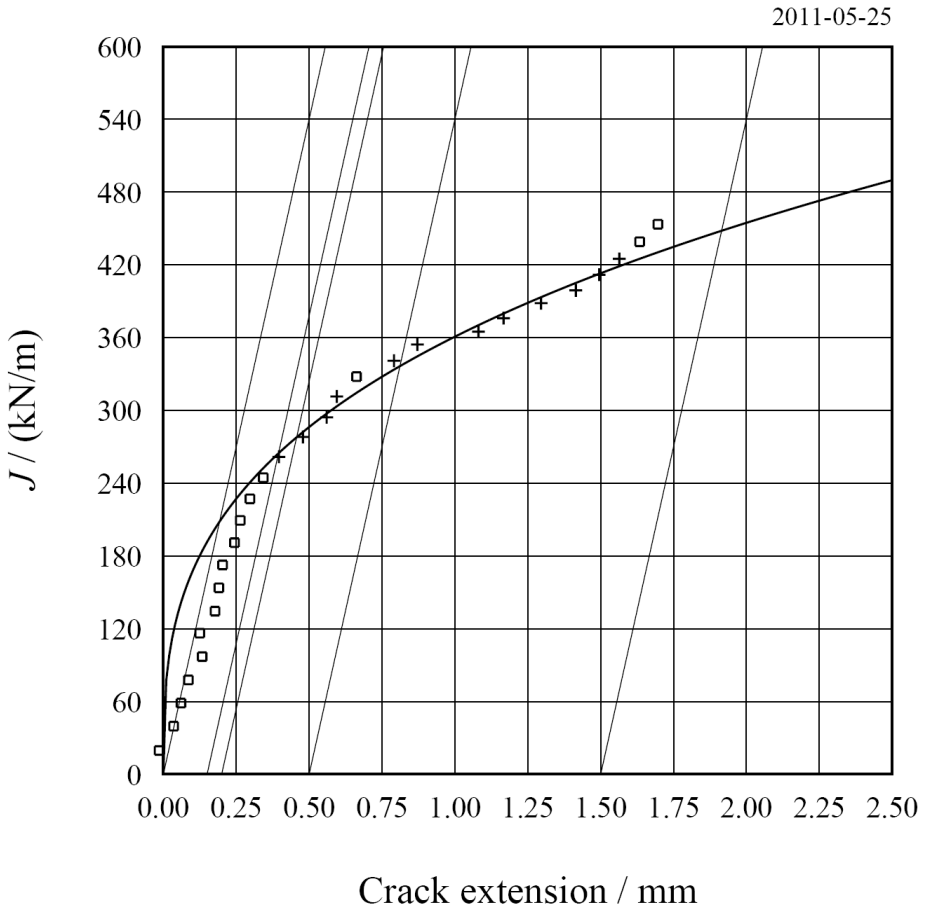

FRACTURE TOUGHNESS TEST - J_{Ic} according to ASTM E 1820

Specimen no.	15835J			
Label	D3			
Task	Bolinder			
Type	SENB	W=26.95 mm	B=13.48 mm	B_n=10.67 mm
Material	A533B-1			
Temperature	rt °C			
Yield stress	540 MPa			
Precracking max	14 kN			
Loading rate	1.75 (Limit load)/(minute)			
Fatigue crack	13.62 mm			
Max. crack deviation	0.22			
Crack extension	2.26 mm			
Estimated a0q	13.53 mm			

J_{crit} = 248 kN/m

- final crack front too curved

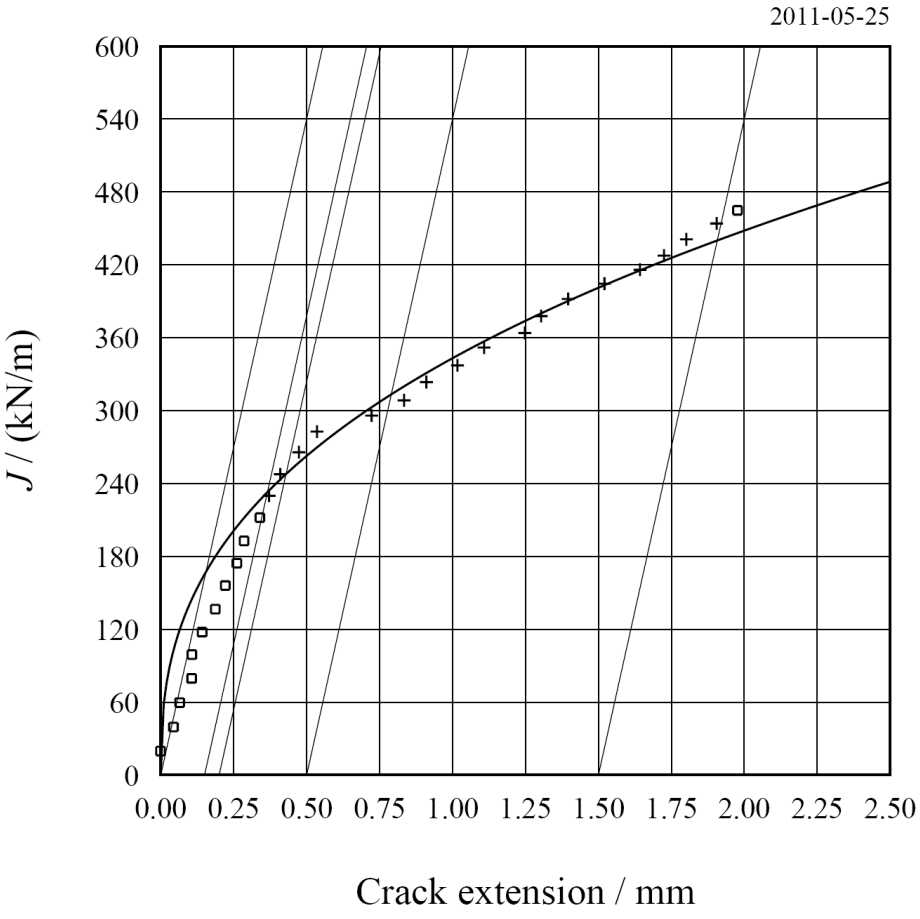

FRACTURE TOUGHNESS TEST - J_{Ic} according to ASTM E 1820

Specimen no.	15836j			
Label	D3			
Task	Bolinder			
Type	SENB	W=26.95 mm	B=13.46 mm	B_n=10.80 mm
Material	A533B-1			
Temperature	rt °C			
Yield stress	540 MPa			
Precracking max	14 kN			
Loading rate	1.80 (Limit load)/(minute)			
Fatigue crack	13.66 mm			
Max. crack deviation	0.28			
Crack extension	2.30 mm			
Estimated a0q	13.60 mm			

J_{crit} = 238 kN/m

- crack extension measurement error = 0.212 mm too high

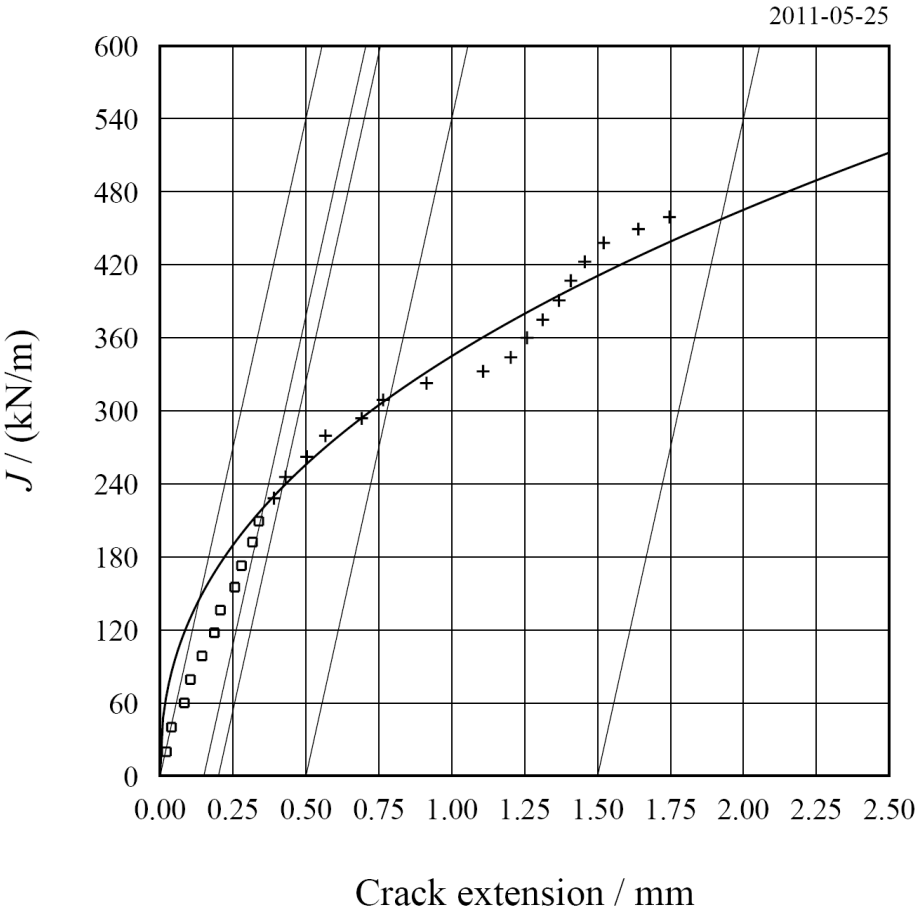

FRACTURE TOUGHNESS TEST - J_{Ic} according to ASTM E 1820

Specimen no.	15837J			
Label	D6			
Task	Bolinder			
Type	SENB	W=26.96 mm	B=13.46 mm	B_n=10.72 mm
Material	A533B-1			
Temperature	rt °C			
Yield stress	540 MPa			
Precracking max	14 kN			
Loading rate	1.74 (Limit load)/(minute)			
Fatigue crack	13.66 mm			
Max. crack deviation	0.19			
Crack extension	2.56 mm			
Estimated a0q	13.60 mm			

J_{crit} = 137 kN/m

- final crack front too curved
- crack extension measurement error = 0.207 mm too high

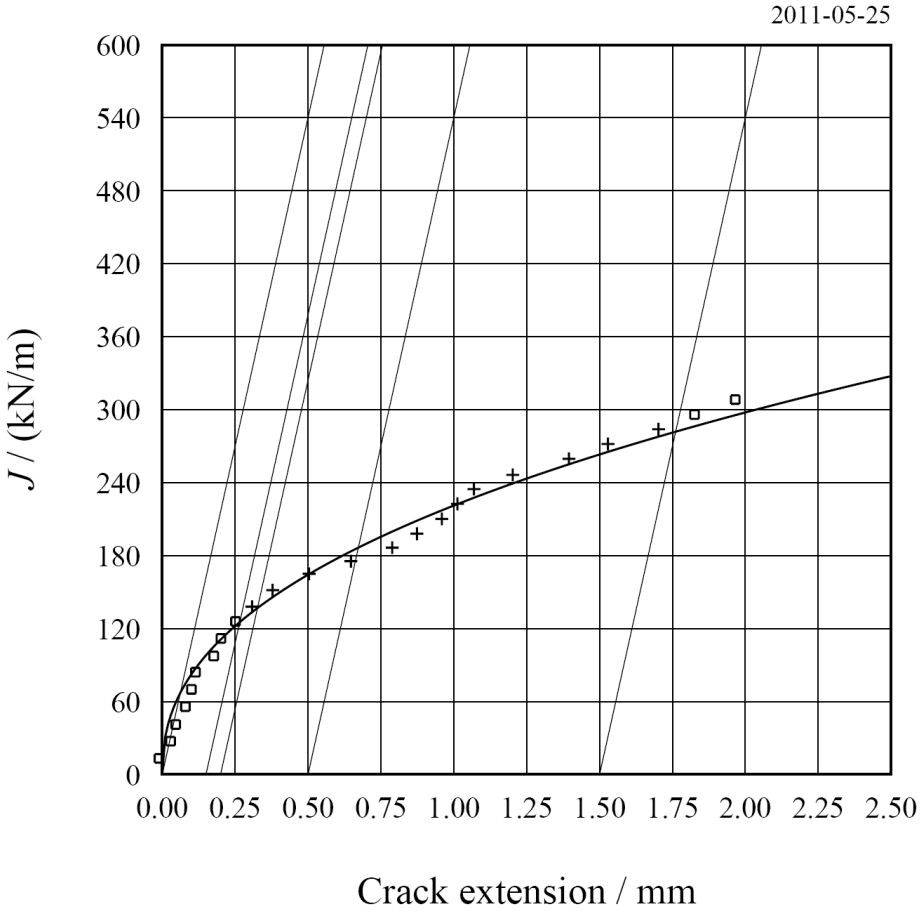

FRACTURE TOUGHNESS TEST - J_{Ic} according to ASTM E 1820

Specimen no.	15838j			
Label	D6			
Task	Bolinder			
Type	SENB	W=26.98 mm	B=13.46 mm	B_n=10.74 mm
Material	A533B-1			
Temperature	rt °C			
Yield stress	540 MPa			
Precracking max	14 kN			
Loading rate	1.72 (Limit load)/(minute)			
Fatigue crack	13.60 mm			
Max. crack deviation	0.23			
Crack extension	2.62 mm			
Estimated a0q	13.58 mm			

J_{crit} = 152 kN/m

- crack extension measurement error = 0.573 mm too high

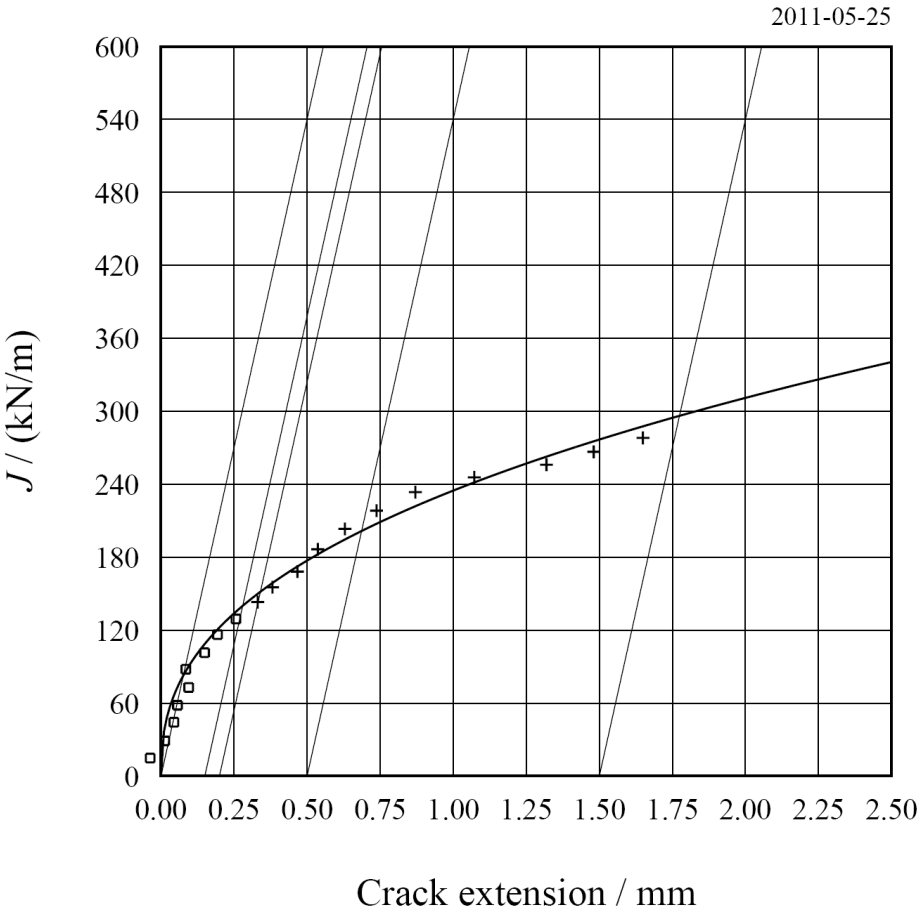

2014:28

The Swedish Radiation Safety Authority has a comprehensive responsibility to ensure that society is safe from the effects of radiation. The Authority works to achieve radiation safety in a number of areas: nuclear power, medical care as well as commercial products and services. The Authority also works to achieve protection from natural radiation and to increase the level of radiation safety internationally.

The Swedish Radiation Safety Authority works proactively and preventively to protect people and the environment from the harmful effects of radiation, now and in the future. The Authority issues regulations and supervises compliance, while also supporting research, providing training and information, and issuing advice. Often, activities involving radiation require licences issued by the Authority. The Swedish Radiation Safety Authority maintains emergency preparedness around the clock with the aim of limiting the aftermath of radiation accidents and the unintentional spreading of radioactive substances. The Authority participates in international co-operation in order to promote radiation safety and finances projects aiming to raise the level of radiation safety in certain Eastern European countries.

The Authority reports to the Ministry of the Environment and has around 315 employees with competencies in the fields of engineering, natural and behavioural sciences, law, economics and communications. We have received quality, environmental and working environment certification.

Strålsäkerhetsmyndigheten
Swedish Radiation Safety Authority

SE-171 16 Stockholm
Solna strandväg 96

Tel: +46 8 799 40 00
Fax: +46 8 799 40 10

E-mail: registrator@ssm.se
Web: stralsakerhetsmyndigheten.se